

**Lecture “Characterization of Solid Catalysts and
Functional Materials“
by apl. Prof. Dr. Michael Hunger**

| | | |
|--|--|--------------------------|
| Institute of Chemical Technology University of Stuttgart | Characterization of Solid Catalysts and Functional Materials | Prof. Dr. Michael Hunger |
|--|--|--------------------------|

Contents of the Lecture

1. Introduction
2. Microscopy methods
 - 2.1 Electron microscopy
 - 2.1.1 Basics of electron microscopy
 - 2.1.2 Experimental techniques of electron microscopes
 - 2.1.3 Application of imaging electron microscopy
 - 2.2 Atomic force microscopy (AFM)
 - 2.2.1 Basics of atomic force microscopy
 - 2.2.2 Experimental technique of atomic force microscopes
 - 2.2.3 Application of atomic force microscopy
 - 2.3 Scanning tunnel microscopy (STM)
 - 2.3.1 Basics of scanning tunnel microscopy
 - 2.3.2 Experimental techniques of scanning tunnel microscopes
 - 2.3.3 Application of scanning tunnel microscopy
3. Diffraction methods
 - 3.1 X-ray diffraction (XRD)
 - 3.1.1 Basics of X-ray diffraction
 - 3.1.2 Experimental technique of X-ray diffraction
 - 3.1.3 Application of X-ray diffraction
 - 3.2 Low energy electron diffraction (LEED)
 - 3.2.1 Basics and experimental technique of electron diffraction
 - 3.2.2 Application of electron diffraction
 - 3.3 Neutron diffraction (ND)
 - 3.3.1 Basics of neutron diffraction
 - 3.3.2 Experimental technique of neutron diffraction
 - 3.3.3 Application of neutron diffraction
4. X-ray absorption spectroscopy (XAS)
 - 4.1 Basics of XANES and EXAFS
 - 4.2 Experimental technique of X-ray absorption spectroscopy
 - 4.3 Application of X-ray absorption spectroscopy
5. Electron spectroscopy
 - 5.1 Basics of electron spectroscopy
 - 5.2 X-ray photoelectron spectroscopy (XPS)

- 5.2.1 Basics and experimental technique of X-ray photoelectron spectroscopy
- 5.2.2 Application of X-ray photoelectron spectroscopy
- 5.3 Ultraviolet photoelectron spectroscopy (UPS)
- 5.3.1 Basics and experimental technique of ultraviolet photoelectron spectroscopy
- 5.3.2 Application of ultraviolet photoelectron spectroscopy
- 5.4 Auger electron spectroscopy (AES)
- 5.4.1 Basics and experimental technique of Auger electron spectroscopy
- 5.4.2 Application of Auger electron spectroscopy
- 6. Ion spectroscopy
 - 6.1 Basics of ion spectrometry
 - 6.2 Secondary ion mass spectrometry (SIMS)
 - 6.2.1 Basics and experimental technique of SIMS
 - 6.2.2 Application of SIMS
 - 6.3 Secondary neutral mass spectrometry (SNMS)
 - 6.3.1 Basics and experimental technique of SNMS
 - 6.3.2 Application of SNMS
 - 6.4 Rutherford backscattering (RBS)
 - 6.4.1 Basics and experimental technique of Rutherford backscattering
 - 6.4.2 Application of Rutherford backscattering
 - 6.5 Low energy ion scattering (LEIS)
 - 6.5.1 Basics and experimental technique of low energy ion scattering
 - 6.5.2 Application of low energy ion scattering
- 7. Vibrational spectroscopy
 - 7.1 Basics of vibrational spectroscopy
 - 7.2 Infrared spectroscopy (IR)
 - 7.2.1 Basics and experimental technique of IR spectroscopy
 - 7.2.2 Application of IR spectroscopy
 - 7.3 Raman spectroscopy
 - 7.3.1 Basics and experimental technique of Raman spectroscopy
 - 7.3.2 Application of Raman spectroscopy
 - 7.4 Electron energy loss spectroscopy (EELS)
 - 7.4.1 Basics and experimental technique of EELS
 - 7.4.2 Application of EELS
- 8. UV/Vis and EPR spectroscopy
 - 8.1 Comparison of both methods
 - 8.2 UV/Vis spectroscopy
 - 8.2.1 Basics and experimental technique of UV/Vis spectroscopy
 - 8.2.2 Application of UV/Vis spectroscopy

- 8.3 EPR spectroscopy
 - 8.3.1 Basics and experimental technique of EPR spectroscopy
 - 8.3.2 Application of EPR spectroscopy
- 9. Solid-state NMR spectroscopy
 - 9.1 Basics of solid-state NMR spectroscopy
 - 9.2 Experimental technique of solid-state NMR spectroscopy
 - 9.3 Application of solid-state NMR spectroscopy
- 10. Thermal surface characterization methods
 - 10.1 Temperature-programmed reduction (TPR)
 - 10.1.1 Basics of temperature-programmed reduction
 - 10.1.2 Application of temperature-programmed reduction
 - 10.2 Temperature-programmed sulfurization (TPS)
 - 10.2.1 Basics of temperature-programmed sulfurization
 - 10.2.2 Application of temperature-programmed sulfurization
 - 10.3 Temperature-programmed desorption (TPD)
 - 10.3.1 Basics of temperature-programmed desorption
 - 10.3.2 Application of temperature-programmed desorption
 - 10.4 Microcalorimetry
 - 10.4.1 Basics of microcalorimetry
 - 10.4.2 Application of microcalorimetry

Literature

- L1. H.-J. Bautsch, J. Bohm, I. Kleber, *Einführung in die Kristallographie*, Verlag Technik GmbH, Berlin, 1990.
- L2. J.W. Niemantsverdriet, *Spectroscopy in Catalysis*, VCH, Weinheim, 1995.
- L3. J.F. Haw (ed.), *In-situ Spectroscopy in Heterogeneous Catalysis*, Wiley-VCH, Weinheim, 2002.
- L4. H.G. Karge, J. Weitkamp (eds.), *Molecular Sieves: Science and Technology, Characterization I*, Springer, Berlin, 2004.
- L5. B.M. Weckhuysen (ed.), *In-situ Spectroscopy of Catalysts*, American Scientific Publishers, Stevenson Ranch, 2004.
- L6. B.C. Gates, H. Knözinger (eds.), *Advances in Catalysis (Modern Operando Methods)*, Vol. 50, Academic Press, Amsterdam, 2006.
- L7. G. Ertl, F. Schüth, J. Weitkamp, *Handbook of Heterogeneous Catalysis, Vol. 2, Characterization of Solid Catalysts*, Wiley-VCH, Weinheim, 2008.
- L8. D. Haarer, H.-W. Spiess, *Spektroskopie amorpher und kristalliner Festkörper*, Steinkopf, Darmstadt, 1995.

1. Introduction

The goal is a better understanding of heterogeneously catalyzed reactions and of the properties and function of solid catalysts. Modern analytical methods help to find answers on questions like:

- What are the chemical composition, structure, and phase composition of the catalyst framework?
- What is the dispersion and chemical behaviour of metals on support materials or of guest compounds in porous solids?
- What are the nature, chemical behaviour, accessibility, and concentration of the catalytically active sites?
- What is the influence of the oxygen coordination and/or local structure of the active surface sites on their catalytic activity?
- What are the particle size and morphology of solid catalysts and do they influence the catalytic activity?
- What kind of adsorbate complexes is formed by reactants on the surface of solid catalysts?
- What are the intermediates of heterogeneously catalyzed reactions? Are there different reaction steps leading to different reaction products?
- What are the reasons of catalyst deactivation? Are there changes in the local structure and/or blocking of active sites?

There is a number of characterization methods with their abbreviations generally used in literature.

- For a survey and short explanations, see Tab. 1.1

Distinction of characterization methods according to:

- Incident primary beams or primary particles and emitted beams and particles or responses of the samples under study: → Tab. 1.2
- Strength of the interactions of beams and particles or physical effects: → Fig. 1.1

- The interaction energy often correlates with the sensitivity of the method

Survey on characterization methods with different applications, limitations, and possible messages: → Tab. 1.3:

- Penetration depth of beams or particles
- Size of the sampled surface
- Modification/damage of the sample material during the measurement
- Effort for the sample treatment
- Possibility of quantitative studies (e.g. number of surface sites)
- Investigations in the presence of gases, such as reactants
- Available temperature range (studies under reaction conditions)
- Possible messages

Nowadays, studies are often performed under “in situ” conditions (at the natural position, in the natural state, for catalysts) and under “operando” conditions, i.e. with working catalysts like in commercial processes

2. Microscopy methods

Aims for microscopic studies can be, e.g.:

- Clearing up of the morphology and pore structure of solid catalysts
- Determination of the size and distribution of metal clusters on supports
- Investigation of the arrangement of atoms and molecules on surfaces
- Observation of surface complexes and reaction steps

Distinction according to incident particles or primary interactions:

- Electrons as probes (EM: electron microscopy)
- atomic forces between the cantilever tip and the catalyst surface (AFM: atomic force microscopy)
- Tunnel currents between the cantilever tip and the surface atoms of the catalyst (STM: scanning tunneling microscopy)

2.1 Electron microscopy

2.1.1 Basics of electron microscopy

General remarks (L2, p. 166):

- Images of very small particles require electron beams with wavelengths smaller than the characteristic details of the sample material, i.e. high-energetic electrons (2 to 400 keV with λ smaller than 1 nm): → Fig. 1.1
- Electrons are emitted, e.g., at a tungsten filament cathode, which is also called thermo-ionic electron gun
- Other approaches consist in the application of a field emission gun (FEG) with a cold cathode made by tungsten single crystals, which are negatively charged with some kV
- In addition, field emission guns with directly neighboured electrodes, causing a large electric field gradient, are used
- In the case of scanning techniques, the electron beam is directed into condenser lenses system and focused to a narrow beam with a diameter of 0.4 to 5 nm for the scanning of the catalyst surface

Effects of incident primary electrons on the samples under study: → Fig. 2.1

- Formation of X-ray radiation and photons
- Diffraction of electrons at scattering sites deeply inside sample material
- Transmission of electrons
- Energy transfer to atoms of the sample material
- Backscattering of electrons at the sample surface
- Emission of secondary electrons
- Formation of Auger electrons

2.1.2 Experimental techniques of electron microscopy

Schematic description of TEM, SEM, and STEM: → Fig. 2.2

Transmission electron microscope (TEM)

- Comparable with optical microscopy

- A beam of primary electrons, which is large in diameter, is parallel aligned via an electrostatic lenses system and transmitted through the sample material
- Transmitted electrons cause a two-dimensional projection, called image, of the sample
- The attenuation of the electron beam depends on the density and depth of the sample (max. 100 nm)
- Typical primary electrons have energies of 100 to 200 keV
- Vacuum of 10^{-6} mbar is required, resolutions of 0.5 nm, and enlargements of 10^5 bis 10^6 can be reached

Scanning electron microscope (SEM)

- The abbreviation SEM is also used for secondary electron microscopy
- Scanning of the sample surface with a very narrow electron beam
- Penetration depth of 100 nm to 5 μ m
- Formation of secondary (5-50 eV) and backscattered electrons (energy similar to primary electrons)
- Intensities of the secondary and backscattered electrons depend on the position of the primary beam on the sample surface
- Detector measures the electron density used to calculate the sample image
- Resolution of 5 nm
- The electron beam causes a charging of the sample, which must be compensated by a positive potential on the sample

Scanning transmission electron microscope (STEM)

- Combination of TEM and SEM
- Allows the recording of bright field (bf) and dark field (df) images by detection of the directly transmitted electrons and the scattered electrons, respectively

High-resolution transmission electron microscope (HRTEM)

- Utilizing the interference of the scattered and axially transmitted electron for improving the resolution
- Significant enhancement of the contrast due to evaluation of the relative phases of the electron waves inside the beam
- Resolution of up to 0.14 nm (L6)

Sample treatment for electron microscopy (L6):

- For SEM, small sample particles are glued on a conductive support and covered (some nm) by gold vapour
- For TEM, STEM, and HRTEM, the samples should be thinner than 100 nm
- Often, the solid sample material is grind, dispersed in a liquid (e.g. ethanol), and distributed on a carbon film, which is placed on a copper grid
- In other cases, the sample particles are mixed with resin, which is cut to thin slices with a thickness of 10 to 100 nm

Specific equipment for in situ studies in the field of heterogeneous catalysis (L6):

- Differentially pumped electron microscopes allow the adsorption of gases on the sample (up to 15 mbar, simulation of reactants) and the simultaneous evacuation of the electron optics: → Fig. 2.3 (IGP: ion-getter pump, TMP: turbo molecular pump, MDP: molecular diffusion pump, ODP: oil diffusion pump, FEG: field emission gun, C1, C2: condenser apertures, SA: selected area aperture, OL: objective lens)
- Sample holder with heater, thermocouple, and a grid for supporting the sample material, temperature range up to 1470 K: → Fig. 2.4
- Thin-window cell for the investigation of samples with thin gas films at a pressure of up to 200 mbar, which can be transmitted by the electron beam, and at temperatures of up 470 K
- Electron scattering at the window material limits the resolution (L6)

2.1.3 Applications of imaging electron microscopy

- Study of the stacking-sequence of the structure of zeolite ETS-10 (T. Ohsuna et al., *Stud. Surf. Sci. Catal.* 84 (1994) 413): → Fig. 2.5
- Investigation of the dispersion and encapsulation of the metal on Rh/TiO₂ catalysts as a function of the treatment temperature (A.D. Logan et al., *Langmuir* 4 (1988) 827): → Fig. 2.6
- Study of the arrangement of Pt atoms in Pt clusters (L. Cervera et al., *EMAG-NANO 05, Conference Series* 26 (2006) 25): → Fig. 2.7

Evaluation of the interaction of incident primary electrons by spectroscopic methods for chemical analysis: → Fig. 2.8

- Electron microscopes allow position-resolved investigations of the chemical composition, e.g. via the Auger electrons (AES) and X-ray fluorescence (XEDS)
- X-ray fluorescence is also called electron microprobe analysis (EMA), electron probe microanalysis (EPMA), and energy dispersive analysis of X-rays (EDAX, EDX)
- There are two different set-ups for the study of X-ray fluorescence: Using an energy-dispersive detector (EDX) or a wavelength-dispersive spectrometer: → Fig. 2.9
- Quantitative studies require comparison with an external standard
- Since the thickness of the sample strongly influences the obtained results, e.g. formation of secondary electrons (absorption) for a large penetration depth, sample films should be used having a thickness smaller than the penetration depth of the primary electrons (ca. 100 nm)

2.2 Atomic force microscopy (AFM)

2.2.1 Basics of atomic force microscopy

General remarks:

- Detection of the very weak forces between a tip and the sample surface in the order of nano-Newton (nN)
- The tip is fixed on a flexible arm, called cantilever, which can be moved in a sub-nanometer scale

Three working regimes are distinguished: → Fig. 2.10

a) Contact mode

- Application of a very sharp tip
- Evaluation of the interactions (e.g. of electron orbitals) between individual atoms of the tip and the sample surface having a distance of few Å

b) Non-contact mode

- Application of a plump tip

- Evaluation of long-range interactions over a distance of 20 to 300 Å, e.g. electrostatic or magnetic interactions

c) Tapping mode, also called dynamic force mode

- Combination of (a) and (b)
- Cantilever is excited to an oscillation with frequencies of 10 to 500 kHz and amplitudes of 100 to 200 nm
- The scanned image depends on the short-time contacts of the tip with the surface
- The scanning procedure can slightly modify the sample material

2.2.2 Experimental technique of atomic force microscopes

The set-up of an AFM: → Fig. 2.11, left

- Sharp tip on a cantilever with a mirror optics
- Laser and diode array for the detection of the angle variation of the cantilever, caused by its up and down over the sample surface
- Sample holder on the piezoelectric scanner, which allows a positioning and scanning of the sample surface by changing the electric potential at the piezoelectric crystals
- Commercial super-tips are made by silicon or silicon nitride having a radius at the peak of ca. 20 nm
- The shape of the tip strongly influences the quality of the imaging of surface profiles: → Fig. 2.11, right

Advantages and disadvantages:

- There is no specific sample treatment necessary for AFM, also no vacuum as in the case of electron microscopy, i.e. adsorption of reactants is possible, also the presence of solutions
- Can have higher resolution in comparison with SEM
- Delivers three-dimensional images of the sample surface
- Maximum surface elevations, which can be scanned, are in the order of few µm

- AFM can scan surfaces of ca. $150 \times 150 \mu\text{m}$ in comparison with some mm in the case of SEM
- Scanning time of AFM is in the order of minutes and can lead to thermal effects in the samples
- AFM studies can modify and damage the samples under study, especially in the case of contact and tapping mode

2.2.3 Applications of atomic force microscopy

Investigation of the agglomeration of Pt particles on a SiO_2 surface as a function of the temperature (R. Erlandsson et al., *J. Vac. Sci. Technol.* B9 (1991) 825): → Fig. 2.12

2.3 Scanning tunnel microscopy (STM)

2.3.1 Basics of scanning tunnel microscopy

General remarks:

- Tunneling of electrons between a very sharp and electrically charged tip and the surface atoms of the sample under study: → Fig. 2.13
- The tunneling current is a function of the tip-surface distance: → Fig. 2.13, right
- Up and down (z direction) of the tip is performed in such a manner that the tunnelling current remains constant
- The image of the sample surface is a description of the distribution of the Fermi levels of the surface atoms

2.3.2 Experimental technique of scanning tunnel microscopy

Set-up of a STM equipment: → Fig. 2.14:

- A piezo crystal allows a variation of the tip-surface distance
- Electronic equipment for measuring the tunnel current and for the positioning of the piezo-tip cantilever
- The electric potential between the tip and the sample surface is in the order of ca. 100 mV, the tunnel current is 10 to 1000 pA

- The piezo-scanner is combined with the piezo-tip moving the tip over the sample surface
- A computer calculates the image base on the scanning data (x, y) and the tunnel currents

2.3.3 Application of scanning tunnel microscopy

STM image of a Pd surface covered by hydrogen atoms (T. Mitsui et al., *Nature* 422 (2003) 705): → Fig. 2.15

- The image was recorded at 37 to 65 K with 75 s per frame
- The hydrogen atoms (diameter of 15 pm) cause the network in the background
- White dots (diameter of 50 pm) are caused by mobile hydrogen vacancies

3. Diffraction methods

3.1 X-ray diffraction (XRD)

3.1.1 Basics of X-ray diffraction

General remarks (L1, p. 331):

- In 1885, Wilhelm Conrad Röntgen observed the transmitting properties of X-rays, which were called Röntgen rays in Germany
- X-rays are electromagnetic radiations with an energy of 5 to 500 keV and wavelengths of 10^{-9} (near ultraviolet radiation) to 10^{-12} m (near γ -radiation)
- The most important X-rays (K_{α} , K_{β} , K_{γ}) are formed due to the transition of electrons from the L to the K shell, → Fig. 3.1a and 3.1b
- For this purpose, electrons irradiated in a strong electrostatic field at the anode metal cause holes in the K shell of this material
- Construction of a X-ray tube for voltages of 10 to 60 kV: → Fig. 3.2
- The metal type of the anode in the X-ray tube determines the wavelength of the radiation: → Tab. 3.1
- With filters (1), the K_{β} radiation can be blocked, which is important for improving the resolution of X-ray patterns

Diffraction methods:

- Elastic scattering of monochromatic X-ray at atoms of an ordered lattice: → Fig. 3.3
- Constructive interferences allow the calculation of lattice distances d via Bragg's equation $n\lambda = 2d \sin\Theta$ (λ : X-ray wavelength; n : number of the reflex, Θ : scattering angle)
- Via the Scherrer equation, the size $\langle L \rangle$ of a crystal can be calculated in dependence on the width b of the reflection

$$\langle L \rangle = K\lambda / (b \cos\Theta)$$

with the equipment constant K (requires comparison with standard)

3.1.2 Experimental technique of X-ray diffraction

Single crystal technique:

- Irradiation on a single crystal leads to a Laue diagram, which can be observed on a fluorescence screen behind (transition technique) or in front (backscattering technique) of the sample
- The latter technique is used for very large and strongly absorbing crystals
- The Laue diagram (Fig. 3.4) is a dot pattern, which corresponds to the reciprocal lattice of the crystal (see Figs. 3.14 and 3.15 in Section 3.2.1)
- Via this dot pattern, the atoms positions in single crystals can be determined

Powder technique:

- For a random distribution of small crystals in a powder, the dot pattern is transformed into circles with opening angles of 2ν (or $\nu = \Theta$) related to the direction of the incident beam: → Fig. 3.5
- During the recording of the circles, the sample is rotated for reaching a better distribution of the crystal orientations (Debye-Scherrer method): → Fig. 3.6
- Only crystals in a specific orientation contribute to the interference
- The film or diode array on the screen (→ Fig. 3.7) show the different series of interference circles

Bragg-Brentano technique: → Fig. 3.8:

- Scheme of a routine laboratory XRD equipment

- The powder sample is fixed on the focusing circle
- In this case, the divergent X-ray beam is focused on a slit in front of the detector
- The X-ray source and the detector are moved in the angle range 2θ
- Large sample surfaces allow high scanning rates
- Due to the divergence and the wavelength distribution of X-rays of X-ray tubes (high linewidth), the resolution of the recorded patterns is limited

Using synchrotrons as X-ray sources: → Figs. 3.9 and 3.10:

- Allow an improvement of the resolution of the patterns by decreasing the full width at half maximum (FWHM) of the reflections
- Advantages are (i) high beam intensity, (ii) small divergence of the beam, and (iii) adjustable wavelength
- In this case, single crystals with a diameter of few μm can be investigated

Evaluation of X-ray powder patterns via Rietveld refinement:

- Developed in 1969 by Hugo Rietveld, *J. Appl. Crystallogr.* 2 (1969) 65
- Comparison of the calculated intensity distribution function y_i of the reflections i of an assumed model crystal with the experimentally derived diffraction pattern and step-wise approximation

$$S_y = \sum_i w_i [y_i(\text{obs}) - y_i(\text{calc})]^2$$

by minimizing the mean quadratic deviation

- The term $y_i(\text{calc})$ includes a number of parameters of the above-mentioned model crystal, such as:
 - Peak profiles, often obtained via reference samples
 - Space group
 - Geometric limitations (atom connectivity, atom-atom distances, T-O-T bond angles, pore diameters etc.)

Limitations of X-ray diffraction:

- Due to the divergence and wavelength distribution of X-ray tubes and the low intensity of the laboratory X-ray equipment
- Limitations in the resolution of diffraction patterns due to small crystals

- Preferred orientations of crystals, e.g. in the case of very flat shapes, lead to distortions of the relative intensities of the reflections

3.1.3 Application of X-ray diffraction

In situ study of the phase transition of a solid catalyst (H. He et al., *Chem. Phys. Lett.* 196 (1992) 267): → Fig. 3.11:

- Use of hard X-ray beams with an energy in the range of 15 to 80 keV at the synchrotron in Daresbury
- Development of a high-temperature cell with an energy dispersive detector
- Sample is rotated for reaching a better random orientation of the sample material
- The main block is made by copper and can be heated
- The energy dispersive detector is fixed at $2\Theta = 1.9^\circ$
- Equipment allows determination of lattice distance d in the range of 0.45 to 2.5 nm
- At 423 to 429 K, the pattern of VPI-5 (18-ring aluminophosphate) is transformed within 30 minutes into the pattern of AlPO₄-8 (10-ring aluminophosphate)

3.2 Low energy electron diffraction (LEED)

3.2.1 Basics and experimental technique of electron diffraction

General remarks: → Fig. 3.13:

- Elastic (without exchange of energy) scattering of a beam of mono-energetic electrons at the surface of a crystalline solid under high-vacuum conditions
- Electron energies of 50 to 200 eV
- Low penetration depth and, therefore, mainly scattering at the outer surface or only at a depth of few atom layers
- Wavelength λ of electrons is (wave-particle duality)

$$\lambda = h / \sqrt{2m_e E_{kin}}$$

with the electron mass m_e and the kinetic energy E_{kin} of the electrons

- Analogous to the Bragg equation of X-ray diffraction is

$$n\lambda = a \sin \alpha$$

with the distance a between two atoms (for α see Fig. 3.13)

- Determination of the scattering angle via a fluorescence screen, film or counter tube

Interpretation of LEED patterns:

- Similarly like in the case of a Laue diagram, the LEED pattern gives a reciprocal lattice
- Definition of the unit vectors of a reciprocal lattice: → Fig. 3.14
- The smaller atom-atom distances in a specific direction in the real lattice give the larger dot distances in the LEED pattern
- Examples for different atomic arrangements in lattices: → Fig. 3.15

3.2.2 Application of electron diffraction

Investigation of the effect caused by the oxidation of rhodium single crystal on the atom arrangement in this material (J.I. Flege, P. Sutter, *Phys. Rev. B* 78 (2008) 153402): → Fig. 3.16

- The pattern in (a) is a monoatomic rhodium layer, which is covered by a monoatomic oxygen-adlayer phase
- After the phase transition, the pattern (b) corresponds to a O-Rh-O three-layer oxide at the surface
- In (c), the time dependence of the (01) reflex at $h = 0.92$ is shown (r.l.u. at the axis corresponds to “reciprocal lattice units”)

3.3 Neutron diffraction (ND)

3.3.1 Basics of neutron diffraction

General remarks:

- Meanwhile, various neutron sources with high beam densities are, e.g. at the Institute Laue-Langevin in Grenoble
- According to Broglie's equation, neutrons have a wavelength of (wave-particle duality)

$$\lambda = h / m_n v_n$$

with the neutron mass m_n and the neutron velocity v_n

- The wave vector k , momentum $p = m_n v_n = \hbar k$, and energy E of the neutrons are related according to: $E = \frac{1}{2} m_n v_n^2 = \hbar^2 k^2 / 2m_n = \hbar^2 / 2m_n \lambda^2$
- In neutron diffraction, coherent scattering of neutrons, which leads to constructive interferences, and incoherent scattering are distinguished (in the latter case, neutrons cause no coherently related waves)
- For cross sections σ of the coherent and incoherent neutron scattering and neutron absorption ($\langle b \rangle$: mean scattering length), see Tab. 3.2
- σ corresponds to the probability P of scattering or absorption at a site

$$P = z \sigma / S$$

with the number z of the sites and the area S

- The value of the coherent cross section is very similar for H (or D), Si, Al, and O, i.e. organic adsorbate molecules are visible for neutron diffraction
- Elastic scattering of coherent neutrons is used for structure determination, but the incoherently scattered neutrons cause sometimes a problematic background
- Quasi-elastic and inelastic neutron scattering can be used for studying molecular mobility (rotation, diffusion) and the excitation of vibrations, respectively

3.3.2 Experimental technique of neutron diffraction

Time-of-flight neutron spectrometer IN6, → Fig. 3.17:

- One of ten instruments in Grenoble
- Works with cold neutrons having a wavelength of 0.4 to 0.6 nm
- Resolution of 70 to 200 μeV or 0.51 to 1.61 cm^{-1}
- By three monochromators, monochromatic neutron beams with different wavelengths are produced
- A beryllium filter suppresses reflected neutrons
- Choppers cut the continuous neutron beam into neutron pulses
- At the detector screen, 337 He^3 detectors are arranged in an angle range of 10 to 115°
- In addition, the time-of-flight is evaluated for determining the neutron energy
- The difference of the wave vector in front (k_0) and behind (k') of the sample gives the neutron transfer momentum Q

3.3.3 Application of neutron diffraction

Example for the application of elastic neutron diffraction:

- Neutron diffraction at zeolite Na-Y, which was loaded with benzene molecules (A.N. Fitch et al., *J. Phys. Chem.* 90 (1986) 1311): → Figs. 3.18 and 3.19:
- dehydrated Linde zeolite Na-Y was loaded with 1.1 and 2.6 molecules C₆D₆ per supercage (s.c.)
- Diffraction studies were performed at 4 K with neutrons having a wavelength of 1.909 and 2.980 Å using the D1A neutron diffractometer in Grenoble
- Recording of the neutron diffraction patterns in the angle range of 2Θ = 6 to 158° in steps of 0.05° and taking 18 h per pattern
- Structure calculations according to the Rietveld procedure gave for 1.1 C₆D₆/s.c. benzene positions in the centers of the supercage and in the centers of the 12-ring windows
- For a loading of 2.6 C₆D₆/s.c., formation of ordered benzene clusters was found

Examples for the quasi-elastic (QENS) and inelastic neutron scattering (INS):

- In the case of inelastic neutron scattering, energy is exchanged with the scattering site: → Fig. 3.20, left
- The energy transfer leads to an excitation of vibrations, mostly of the H atoms due to their large incoherent cross section
- For INS -spectra of TMA⁺ ions in zeolite, see P. Newsam et al., *ACS Symp. Ser.* 437 (1990) 25: → Fig. 3.21
- In the case of quasi-elastic neutron scattering, a broadening of the signal feets occurs: → Fig. 3.20, right
- This broadening indicates a mobility (e.g. diffusion) of the scattering sites
- In the case of translatoric motion, the peak has the shape of a Lorentzian function

$$S = \frac{1}{\pi} \frac{DQ^2}{\omega^2 + (DQ^2)^2}$$

where DQ² is the full width half maximum of the peak, Q the neutron transfer momentum, D the diffusion coefficient, and $\hbar\omega$ is the neutron energy

- For an example of a broadening of diffraction peaks obtained for neutron diffraction on CH_3OH in zeolite H-ZSM-5 at 335 K, see H. Jobic et al., *J. Phys. Chem.* 90 (1986) 1059: → Fig. 3.22
- Peaks were recorded at IN6 in Grenoble with a neutron wavelength of $\lambda = 5.1 \text{ \AA}$ for two scattering angles, which for determining the neutron transfer momentum at different angles
- A diffusion coefficient of $D = 2.8 \times 10^{-5} \text{ cm}^2\text{s}^{-1}$ was determined for CH_3OH in H-ZSM-5

4. X-ray absorption spectroscopy (XAS)

4.1 Basics of XANES and EXAFS

General remarks (L4, p. 427):

- Synchrotrons deliver X-ray beams with high intensity and tunable energy
- They allow detailed investigations of the X-ray absorption edge, which occurs if the X-ray energy excites core level electrons in the L or K shell
- This corresponds to a photo-ionization of the absorbing atom
- In this case, X-ray energies of some keV are required; X-rays of commercial tubes are too weak and not tunable in the X-ray energy

XAS includes the following method: → Fig. 4.1:

a) X-ray absorption near-edge structure (XANES)

- Region of ca. -10 eV to +50 eV related to the edge energy E_0
- This is a region with strong variations of the X-ray absorption
- Absorption combined with transfer of core level electrons to non-occupied outer orbitals causes pre-edge peaks: → Fig. 4.1a
- Gives information on the atoms and their chemical nature in the local structure of the scattering atoms
- The high-energy XANES region is affected by multiple-scattering processes of photoelectrons (difficult evaluation): → Fig. 4.1b

b) Extended X-ray absorption fine structure (EXAFS)

- Region of ca. +50 eV to +1000 eV above the edge energy E_0
- Shows weak oscillations of the absorption
- The excited electrons leave the absorbing atoms

- Photoelectrons can be considered as waves (wave-particle duality), which are scattered at neighbouring atoms: → Fig. 4.1c
- Constructive and destructive interferences of the photoelectron waves emitted by the absorbing atoms and of the waves of electron scattered at neighbouring atoms: → Figs. 4.1d and 4.1e
- Oscillations are a function of the atom-atom distances and the type and number of scattering sites

c) Surface extended X-ray absorption fine structure (SEXAFS)

- Selective investigation of atoms at the surface of a solid material by studying, e.g. the X-ray absorption edge of carbon, nitrogen or oxygen at ca. 285, 400, and 530 eV, respectively

d) Near-edge X-ray absorption fine structure (NEXAFS)

- Investigation of the near-edge X-ray absorption fine structure like EXAFS
- The fine structure of NEXAFS arises from excitations into non-occupied molecular orbitals
- Is used for studying molecules adsorbed at solid surfaces

Advantages and disadvantages:

- While diffraction methods determine the structure and long-range orders, the XAS methods analyse the local environment of the absorbing atoms
- Therefore, the method is also available for amorphous materials
- Also study of the local structure of atoms, which are incorporated in a non-ordered manner as defect sites or impurities in crystalline materials, such as Al, B or Ga in zeolites
- XAS requires synchrotrons with tunable X-ray energy

4.2 Experimental technique of X-ray absorption spectroscopy

a) Standard experiment: → Fig. 4.2a

- Electron or positron storage rings are used as X-ray sources
- Monochromators consisting of Si or Ge single crystals, which separate and filter X-ray with different energies
- Study of the samples in the transmission mode

- Measurement of the beam intensity in front and behind the samples via an ionization chamber
- Samples should be homogeneous and constant in the thickness
- Grinding of samples to a fine powder and mixing, e.g., with boron nitride or polyethylene
- Thickness d of the sample should have such a value that the product of $\mu \cdot d$ (μ : linear absorption coefficient) is in the range of 0.5 to 1.2

b) Detection of the X-ray fluorescence: → Fig. 4.2b

- Used in the case of very thick samples with bad X-ray transmission properties
- An energy dispersive detector or a detector with specific filters determines the X-ray fluorescence as a function of the wavelength of the primary X-ray radiation

c) Detection of photoelectrons: → Fig. 4.2c

- Used in the case of samples with bad transmission properties or application of SEXAFS
- SEXAFS works with very low beam intensities (absorption at the surface)
- Measurement of photoelectrons requires ultra-high vacuum
- Specific detector for photoelectrons

Evaluation of the experiments:

a) XANES

- Oscillations at $E_0 - 10$ eV to $E_0 + 50$ eV are difficult to evaluate
- Position of the pre-edge peak depends on the chemical composition, the oxidation state, and local structure (e.g. oxygen coordination) in the vicinity of the absorbing atoms
- The absorption curve gives a fingerprint of all absorbing atoms
- Quantitative fit of the pre-edge peak by linear combination of the pre-edge peaks obtained for reference materials

b) EXAFS

- Calculation of the EXAFS function $\chi(E)$ via transformation into the k -vector system with k as wave vector

$$k = [(2m_e / \hbar^2)(E - E_0)]^{1/2}$$

and the electron mass m_e

- Simple form of EXAFS function $\chi(E)$ is

$$\chi(k) = \sum_j Amp_j(k) \cdot \sin(2 \cdot k \cdot R_j + \phi_j(k))$$

where R_j is the distance between the absorbing atom and the scattering atoms with summation over all scattering atoms j , the phase shift function $\phi_j(k)$, and the amplitude function $Amp_j(k)$ of the EXAFS oscillation

- Determination of the phase shift function $\phi_j(k)$ by evaluation of the EXAFS functions of well-known reference materials

Example for the evaluation of a EXAFS function (L4, p. 427), e.g. of the experimentally derived EXAFS curve of an unknown gallosilicate (a); the well-known material $ZnGa_2O_4$ was used as reference (b): → Fig. 4.3

1. Subtraction of the background signals, i.e., the curves obtain a baseline at zero level before the absorption edge (c)
2. Transformation into the k space (d, e)
3. k^n -weighting (in the present case $n = 3$) enhances the amplitudes for higher k values (f, g)
4. Fourier transformation into the R space gives the radial distribution function (h, i)
5. Back transformation into the k -vector system for selected R values (see arrows in (j) und (k))
6. Determination of the phase shift function $\phi_j(k)$ for $ZnGa_2O_4$, since the Ga-O-distance ($R_{GaO} = 1.99 \text{ \AA}$) for this material is known,
7. Application of the experimentally obtained phase shift function $\phi_j(k)$ on the EXAFS function of the unknown gallosilicate (l), and determination of $R_{GaO} = 1.83 \text{ \AA}$ (and other parameters) for this material

4.3 Application of X-ray absorption spectroscopy

XANES studies of titanium in a titanosilicate: → Figs. 4.4. and 4.5:

- Determination of the coordination of titanium in the titanosilicalite TS-1 (P. Behrens et al., *J. Chem. Soc. Chem. Commun.* (1991) 678)
- TS-1 has a MFI structure, like zeolite ZSM-5, with tetrahedral silicon sites
- XANES measurements with HASYLAB at DESY in Hamburg

- Pre-edge peak is caused by an excitation of 1s electrons and their $1s \rightarrow 3d$ transition (E_0 in the picture is set to zero)
- Reference samples deliver characteristic fingerprints
- Fit of the pre-edge peak of TS-1 using the pre-edge peaks of the reference materials, which gives the following oxygen coordinations for the titanium atoms in TS-1: 10% tetrahedral, 15% square-pyramidal, and 75% octahedral (estimated error of 5%)

XANES studies of copper coordination in zeolite Y: → Fig. 4.6

- Investigation of zeolites Na-Y ($n_{Si}/n_{Al} = 3$), which were exchanged in an aqueous solution of $Cu(NO_3)_2$ and of a zeolite H-Y, which was treated with gaseous $CuCl$ at 573 K (C. Lamberti et al., *Chem. Phys. Lett.* 269 (1997) 500)
- In addition, samples suitable as references for Cu^0 , Cu^+ , Cu^{2+} , and Cu^{3+} , were studied
- Measurements at GILDA of the European Synchrotron Radiation Facility (ESRF) in Grenoble
- XANES region shows pre-peaks due to $1s \rightarrow 3d$ (empty arrows) and $1s \rightarrow 4p$ electron transitions (full arrows)
- Crosses assign the edge energy E_0
- Spectrum (e) of zeolite Y exchanged with $Cu(NO_3)_2$ can be explained by Cu^{2+}
- Spectrum (f) of zeolite Y treated with $CuCl$ indicates the presence of Cu^+
- Spectrum (g) of the above-mentioned zeolite reduced with CO is caused by Cu^0

EXAFS studies of the coordination of molybdenum in zeolite Y (L4, p. 427): → Fig. 4.7

- Loading of zeolite Y with molybdenum and other metals as given in the caption of Fig. 4.7 and treatment with H_2S at maximum 673 K
- Investigation of the Mo K edge at the beam line BL-10B of the Photon Factory in Sendai, Japan, 2 GeV synchrotron
- The radial distribution functions show peaks at $R = 1.3 \text{ \AA}$ for Mo-O, $R \approx 1.9 \text{ \AA}$ for Mo-S, $R \approx 2.3 \text{ \AA}$ for Mo-Co, and $R \approx 2.7 \text{ \AA}$ for Mo-Mo
- High intensity of the Mo-S peak correlates with a high catalytic activity in the hydrodesulfurization: The sample in (b) is much more active than the sample

in (a), lower activity upon Fe modification (c), and increasing activity upon Co modification (d)

EXAFS studies of the local structure of palladium in zeolite (Y Z. Zhang et al.,

Zeolites 10 (1990) 784): → Fig. 4.8, Tab. 4.1

- Investigation of Pd in zeolite Na-Y exchanged with $\text{Pd}(\text{NH}_3)_4^{2+}$ complexes and calcined at 523, 573, and 773 K
- Experiments were performed at the beam line X-18B of NSLS in Brookhaven
- Sample mass of 400 mg
- With increasing calcination temperature, enhanced signals at large R values occur in the radial distribution function (Fig. 4.8, top)
- Fit of the back transformed EXAFS function indicates that Pd is coordinated with N atoms ($N = 2.6$, $R = 2.01 \text{ \AA}$) upon calcination at 523 K: → Tab. 4.1
- Upon calcination at 573 and 773 K, Pd coordinates exclusively and stronger with O atoms
- There are two different oxygen coordination spheres, which can be explained by Pd in the sodalite cages and in the hexagonal prisms of the faujasite structure of the zeolite Y

5. Electron spectroscopy

5.1 Basics of electron spectroscopy

General remarks (L2, p. 37): → Fig. 5.1

- Distinction between XPS (X-ray photoelectron spectroscopy) and UPS (ultraviolet photoelectron spectroscopy)
- Both methods base on the photoelectric effect, i.e., an atom absorbs a photon of the energy $h\nu$ and, subsequently, a core level electron (XPS) or a valence electron (UPS) is emitted
- First photoemission experiments were performed and described 1887 by Hertz, but first Einstein could explain the effect in 1905
- Photoemission of electrons is a surface-sensitive method since the mean free path of electrons in solids is very limited (less than 1 to 2 nm for $E_{\text{kin}} = 15$ to 1000 eV): → Fig. 5.2

5.2 X-ray photoelectron spectroscopy (XPS)

5.2.1 Basics and experimental technique of X-ray photoelectron spectroscopy

General remarks (L2, p. 39):

- Formation of photoelectrons with kinetic energies of 0.2 to 1.5 keV from atom layers in a depth of 1.5 to 6 nm below the surface: → Fig. 5.2
- The XPS equipment consists of an X-ray source, focusing circle with crystal, sample support, electrostatic or magnetic lenses system and detector: → Fig. 5.3
- Detection of electrons requires high-vacuum
- Often, X-rays of Mg K α (1253.6 eV) and Al K α (1486.3 eV) transitions are used
- The kinetic energy E_{kin} of the emitted electrons is

$$E_{\text{kin}} = h\nu - E_b - \varphi \quad \text{or} \quad E_b = h\nu - E_{\text{kin}} - \varphi \quad (\text{plot of the spectrum})$$

with the frequency ν of the incident radiation, the binding energy E_b of the photoelectrons, and the work function φ of the spectrometer

- Spectra correspond to the number of photoelectrons $N(E)$ plotted as a function of the kinetic energy E_{kin} or the binding energy E_b
- XPS signals are involved in a chemical shift, which depends on the oxidation state of the photo-ionized atom: → Tab. 5.1
- For an example of a XPS spectrum, see that of Al₂O₃-supported rhodium, prepared by impregnation of Al₂O₃ with an aqueous RhCl₃ solution, recorded with Al K α radiation (L2, p. 41) in → Fig. 5.4
- Often, XPS spectra are calibrated with C_{1s} = 284.4 eV
- XPS peaks are assigned by the source of the photoelectrons, i.e., by the initial electron level (e.g. 1s)
- Starting with the p orbitals, often the total momentum $j = l + s$ including the orbital momentum l and the spin momentum s is added (e.g. 3p_{3/2}) since a splitting due to different j values is possible
- On the left-hand side of the spectra, Auger electrons can be observed (can be identified by experiments with different X-ray energies)
- The dominating peak occurring very left is due to oxygen Auger electrons with a binding energy of 986 eV corresponding to a kinetic energy of ca. 500 eV (1486 eV – 986 eV ≈ 500 eV) (see Section 5.4)

AR-XPS (angle-resolved XPS): → Fig. 5.5

- Specific method for XPS studies at different atom layer depths
- The penetration depth of X-rays is much larger than the maximum mean free path of the emitted electrons in the solid, i.e., without losing their energy before reaching the detector
- For flat detection angles, the electrons have a longer way through the material and the probability of an energy loss is much higher
- Therefore, the variation of the XPS spectrum for different detection angle gives information on depth of the layers containing the photo-ionized atoms

5.2.2 Application of X-ray photoelectron spectroscopy

XPS studies of pyridine (C_5NH_5) adsorption on zeolites AlPO₄-5, SAPO-5, SAPO-11, SAPO-34, and SAPO-37 (R.B. Borade, A. Clearfield, *J. Mol. Catal.* 88 (1994) 249)

- Upon adsorption of pyridine, samples were evacuated at 10^{-6} bar
- Mg K α radiation with $h\nu = 1253.6$ eV was used and measurement of N_{1s} photoelectrons on a Perkin-Elmer PHI 5500 ESC spectrometer
- Separation of the N_{1s} XPS spectra into two Gaussian curves at different binding energies: → Fig. 5.6
- Signal I is due to pyridine adsorbed at Brønsted acidic sites, while signal II is caused by pyridine adsorbed at Lewis sites
- Quantitative evaluation indicates that the silicoaluminophosphates have much more Brønsted acid sites in comparison with aluminophosphates: → Tab. 5.2

XPS studies of fluorinated Beta zeolites (R.B. Borade, A. Clearfield, *J. Chem. Soc. Faraday Trans.* 91 (1995) 539)

- The NH₄-Beta zeolite was impregnated with different amounts of a 0.1 M NH₄F solution and calcined for 8 h at 723 K: → Tab. 5.3
- Mg K α radiation with $h\nu = 1253.6$ eV was used and F_{1s} photoelectrons were measured on a Perkin-Elmer PHI 5500 ESC spectrometer

- Separation of the F_{1s} XPS spectra into maximum three Gaussian curves at different binding energies: → Fig. 5.7
- Binding energies of ca. 688 eV (species I), 686 eV (species II), and 684 eV (species III): → Tab. 5.4
- Suggested assignments:
 - signal I corresponds to F-Al bondings like in AlF₆³⁻
 - signal II is explained by F atoms at defect sites (F-O) at the outer surface and at pore openings
 - signal III is due to F-Si bondings like in SiF₆²⁻

XPS studies on Cu cations in ZSM-5 zeolites (E.S. Shapiro et al., *Catal. Lett.* 24 (1994) 159)

- Na-ZSM-5 zeolite was exchanged in a 0.1 M Cu(CH₃CO₂)₂ solution and, subsequently, thermally treated under different conditions (material is interesting for cleaning of the exhaust of Otto engines): → Fig. 5.8
- Mg K α radiation with $h\nu = 1253.6$ eV was used and the Cu_{2p3/2} photoelectrons were measured on a VG ESCA3 spectrometer at temperature of 170 to 200 K
- Main peaks (I_p) occurred at ca. 935 eV (single-electron-process) and shake-up satellites (I_s) appeared at ca. 942 eV (multiple-electron-process)
- Shake-up satellites occur if the formation of the photoelectron causes an additional electron transition in the ionized atom, which leads to an energy loss occurring in the spectrum like a higher binding energy)
- The I_s/I_p ratio in the table of Fig. 5.7 is compared with the Cu(I) and Cu(II) contents
- Large intensities I_s of the shake-up satellites correspond to a high Cu(II) and a low Cu(I) content

XPS studies of the partial charges at lattice atoms in microporous aluminosilicates (M. Huang et al., *J. Am. Chem. Soc.*, 114 (1992) 10005)

- Zeolites X, Y, and ZSM-5 modified with different extra-framework cations
- Mg K α radiation with $h\nu = 1253.6$ eV was used on a VG Scientific Escalab Mark II spectrometer
- To prepare an internal calibration standard (Au_{4f7/2} = 84.0 eV), the activated samples were covered by a gold film (gold vapour treatment)

- For zeolites X and Y, the binding energies of the Si_{2p} and O_{1s} signals depend on the type of the extra-framework cations: → Fig. 5.9
- Calculation of the mean partial charges δ at the framework oxygen (i = O) and silicon (i = Si) atoms according to Sanderson's method:

$$\delta_i = (S_{\text{int}} - S_i) / 2.08 S_i^{1/2}$$

with $S_{\text{int}} = (S_{\text{Si}}^p S_{\text{Al}}^q S_{\text{O}}^r S_{\text{M1}}^{n1} S_{\text{M2}}^{n2})^{1/(p+q+r+n1+n2)}$

and the Sanderson electronegativities S_i of the atoms i and the extra-framework cations M1 and M2

- Correlation between O_{1s} and Si_{2p} binding energies and the calculated partial charges δ_{O} and δ_{Si} , respectively: → Fig. 5.10

5.3 Ultraviolet photoelectron spectroscopy (UPS)

5.3.1 Basic and experimental technique of ultraviolet photoelectron spectroscopy

General remarks (I2, p. 60):

- Instead of X-rays, like in the case of XPS, UPS uses UV light with much lower energy for the formation of photoelectrons: → Fig. 5.11
- Often, helium light with energies of 21.2 and 40.8 eV is used as UV source
- Due to the low excitation energy, exclusively valence electrons are excited
- Suitable method for the study of adsorbate molecules at solid surfaces
- Also for UPS, the angle-resolved technique is utilized (vide supra)
- Similarly to XPS, the binding energy of the electrons is calculated in the case of UPS by their kinetic energy E_{kin} at the detector

$$E_{\text{kin}} = h\nu - E_b - \varphi \quad \text{or} \quad E_b = h\nu - E_{\text{kin}} - \varphi \quad (\text{plot of the spectrum})$$

- Electrons, which are emitted from the Fermi level (zero point of the spectrum) have the highest kinetic energy
- Therefore, there is a strong cut-off at higher binding energies in the spectrum: → Fig. 5.12
- Adsorption of molecules at the surface of solids causes an increase of the binding energies of electrons

5.3.2 Application of ultraviolet photoelectron spectroscopy

UPS studies of the chemisorption and dissociation of CO at a Fe(110) surface (L2, p. 65)

- Activation of the Fe(110) surface under high-vacuum conditions upon saturation with CO
- Helium light with 21.2 and 40.8 eV was used as UV source
- Position of the photoelectron signals from the 4σ and $1\pi + 5\sigma$ orbitals of the adsorbed CO molecules indicates their chemisorption on the surface
- Upon thermal treatment of the non-modified sample at 390 K (Fig. 5.13, left), a signal occurs at ca. 5 eV, which is caused by O_{2p} und C_{2p} photoelectrons
- This signal indicates dissociation of CO
- For K-promoted Fe(110), CO dissociation occurs first upon thermal treatment at 500 K

5.4 Auger electron spectroscopy (AES)

5.4.1 Basics and experimental technique of Auger electron spectroscopy

General remarks (L2, p. 68):

- Equipment is similar to that of XPS: → Fig. 5.3
- In the case of AES, however, Auger electrons with much lower energies are detected and occur at much higher binding energies in the spectrum in comparison with XPS photoelectrons: → Fig. 5.4
- Assignment of the Auger electrons is made according to the filled core level electron shell (e.g. K (1s) in Fig. 5.1), the initial shell of the electron filling the empty core level (e.g. L₁ (2s) in Fig. 5.1) and the shell, which was the source of the emitted Auger electron (e.g. L₂₃ (2p) in Fig. 5.1),
- In the above-mentioned case, this gives KLL Auger electrons
- The kinetic energy, e.g., of a KLM Auger transition is: → L2, p. 69

$$E_{\text{kin}} = E_{\text{KLM}} = E_K - E_L - E_M - \delta E - \varphi \quad (\text{plot in the spectrum})$$

with the binding energy E_M of the photoelectrons (here emitted from shell M), an energy shift δE due to relaxation effects, and the work function φ

- AES spectra are plotted in the reversible direction in comparison with XPS and UPS spectra

- Often, AES signals occur on strong slopes of the spectra of secondary electrons; therefore, evaluation via derivation is useful: → Fig. 5.14
- AES signals give information on the chemical bonds (like XPS) since the Auger process includes electrons from the valence level

5.4.2 Applications of Auger electron spectroscopy

Determination of the chemical composition of solid surfaces (L2, p. 75)

- AES spectra were recorded before and after sputtering of the surface (removal of atom layers by irradiation of ion beams) of $\text{ZrO}_2/\text{SiO}_2$ catalysts: → Fig. 5.15
- Determination of the depth profiles of the O, Zr, Si, and C concentrations
- Comparison of (a) and (b) shows that the surface is preferentially covered by zirconium and oxygen

AES studies of aluminum in zeolite catalysts (W. Grünert et al., *J. Phys. Chem.* 98 (1994) 10920)

- Investigation of zeolites with $n_{\text{Si}}/n_{\text{Al}}$ ratios of 1 to 17 in their sodium form
- Evaluation of the intensity and position of the Al KLL signals for studying framework aluminum: → Fig. 5.16
- Decrease of the kinetic energy (increasing binding energy) of the Auger electrons with decreasing Al content in the zeolite framework from Na-A to Na-ZSM-5

Correlation of XPS and AES data for distinguishing and assigning Cu species in zeolites A, X, and Y (G. Moretti, *Zeolite* 14 (1994) 469)

- XPS and AES measurements were performed as described above
- Plotting of the kinetic energies (AES) and binding energies (XPS) of the Auger electrons and XPS photoelectrons, respectively, in a Wagner plot: → Fig. 5.17
- Assignment of Cu species by comparison with characteristic regions, based on Cu(0)-, Cu(I)-, and Cu(II)-containing reference materials, in the Wagner plot (shaded regions)

6. Ion spectroscopy

6.1 Basics of ion spectroscopy

Distinction of 4 methods:

- Secondary ion mass spectrometry (SIMS)
- Secondary neutral mass spectrometry (SNMS)
- Rutherford backscattering (RBS)
- Low energy ion scattering (LEIS)

General remarks (L2, p. 79): → Fig. 6.1

- SIMS, RBS, and LEIS are $\text{ion}_{\text{in}} - \text{ion}_{\text{out}}$ methods, however, they base on different physical effects
- In the case of SIMS, the primary ions sputter the catalyst surface
- SNMS bases on SIMS, but there is an ionization of the secondary neutral particles before their detection
- In the case of RBS, the penetration depth of the high-energetic primary ions into the catalysts surface is some μm
- LEIS is a method with scattering of the primary ions at the surface atoms of a solid
- All above-mentioned methods require high-vacuum, otherwise, the mean free path of the ions would be too short for their detection

6.2 Secondary ion mass spectrometry (SIMS)

6.2.1 Basics and experimental technique of SIMS

General remarks:

- Primary ions with energies of 0.5 to 5 keV sputter atoms, ions, and molecular fragments from the sample surface
- Primary ions are often noble gases, e.g. Ar^+ and He^+ ions
- Secondary particles are separated and measured in mass spectrometers or time-of-flight spectrometers: → Fig. 6.2
- Ions are detected via electron counter tubes, Faraday cups (metal cup used as ion trap) or CCD (charge-coupled device) camera
- Method requires vacuum of ca. 10^{-6} mbar

- Very sensitive surface method for studying depth profiles of the chemical composition with detection limits of ca. 10^{12} to 10^{16} atoms/cm³
- For a survey on advantages and disadvantages, see Tab. 6.1
- Limited in obtaining quantitative results since in the SIMS effects cannot be described in a simple analytical equation
- SIMS is a destructive method

Distinction according the working regimes:

- Static SIMS:
 - low beam densities with primary ion densities of 10^{-10} to 10^{-9} A/cm² or 10^{12} - 10^{13} ions/cm², sometimes as ion pulses
 - therefore, weak destruction of the sample surface
 - sputtering of an atom monolayer requires a couple of hours
 - it is a real surface method
- Dynamic SIMS:
 - significantly higher beam density in comparison with the former case
 - is more a sputtering process
 - therefore, it is more a bulk method
- Charging of the surface can be a serious problem, especially in the case of isolators
- Therefore, low energy electrons are irradiated to the surface to neutralize it

Description of the SIMS intensities:

- Signal intensity I_S of the secondary ions at the detector is:

$$I_S \approx I_P Y R c_{\text{surf}} \eta$$

with the density I_P of the primary ions, the sputter yields Y , the ionization probability R , the surface concentration c_{surf} , and the transmission η of the mass spectrometer (10^{-3}) or time-of-flight spectrometer (10^{-1})

Dependence of the sputter yield Y :

- Covers a range of 1 to 10 and changes strongly for different atoms: → Fig. 6.3
- Depends on:
 - mass of the primary ions; Xe^+ transfers more kinetic energy than Ar^+

- energy (velocity) of the primary ions; there is an optimum, otherwise the penetration depth is too large: → Fig. 6.4, left
- angle Θ of the primary ion beam related to the surface normal: → Fig. 6.4, right
- at the angle of 0° , the penetration depth is so large that primary ions are absorbed in the solid

Ionization probability R^+ for positively charged ions:

- Can be described by:

$$R^+ \propto \exp \{ \varphi - l \} / v$$

with the work function φ of the sample (energies required to liberate electrons, which subsequently neutralize ions), the ionization potential l of the sputtered particles and their velocity v

- The ionization and neutralization of secondary particles depend on their residence time on the surface and, therefore, on their velocity
- Chemical nature of the vicinity strongly influences this parameter, which is called matrix effect: → Tab. 6.2
- The above-mentioned equation gives trends, but quantitative statements are limited
- Detection of atoms in the ppm region

Plotting of SIMS spectra: → L2, p. 82

- Signal intensity I_s of the secondary ions at the detector is plotted as a function of the atom mass, determined via mass spectrometer: → Fig. 6.5
- Signal splitting by isotope effects, e.g. for copper (63 and 65 amu) and antimony (121 and 123 amu), supports the assignment and interpretation since SIMS peaks of different compounds can overlap
- Large values of $R^+ Y_{\text{oxide}}$ for oxides (Tab. 6.2, last column) leads to a high detection sensitivity for these species (matrix effect due to type of chemical bonds)

6.2.2 Application of SIMS

Study of the formation of $\text{ZrO}_2/\text{SiO}_2$ catalysts (A.C.Q.M. Meijers et al., *Appl. Catal.* 70 (1991) 53): → Figs. 6.6 and 6.7

- Upon loading of SiO_2 with $\text{Zr}(\text{OC}_2\text{H}_5)_4$, an interaction of the ethoxy groups with the support occurs
- The SIMS spectra of the fresh catalyst show weak and characteristic signals of ZrOH^+ at 107 ($^{90}\text{ZrOH}^+$ and $^{91}\text{ZrO}^+$) and 111 amu ($^{94}\text{ZrOH}^+$)
- These peaks are due to fragments of ethoxy groups, which become significantly weaker upon calcinations at 200°C
- Signals of Na^+ and In^+ are artefacts, e.g. caused by a film, which was used for pressing of the sample material
- Intensity ratio of the SIMS peaks of ZrO^+/Zr^+ and $\text{ZrO}_2^+/\text{Zr}^+$ in Fig. 6.7 were compared with those of pure reference materials (see dashed lines)
- Until 200°C , the above-mentioned ratio is in the range of that of the $\text{Zr}(\text{OC}_2\text{H}_5)_4$ reference material (Zr-eth)
- Beginning with 300°C , this ratio changes to values corresponding to the ZrO_2 reference (ZrO_2)
- This finding indicates the temperature range of the catalyst formation

Study of the sulfurization of HDS catalysts (hydrodesulfurization processes) basing on $\text{MoO}_3/\text{SiO}_2/\text{Si}(100)$ materials (L2, p. 92): → Fig. 6.8

- MoO_3 was supported on SiO_2 and activated in a gas mixture of H_2S (10%) and H_2 , i.e., it was sulfurized
- By SIMS, the temperature dependence of the transformation of MoO_3 into MoS_2 was studied
- SIMS signals appear in regions characteristic for elementary Mo^+ (92 to 100 amu), molecular MoO^+ ((92 to 100 amu) + 16 amu (oxygen)), and MoO_2^+ clusters ((92 to 100 amu) + 2x16 amu)
- Already at 25°C , an increase of the peak intensities of MoS^+ ((92 to 100 amu) + 32 amu (sulfur)) occurs, i.e., there is an uptake of sulfur by the catalysts
- This effect is accompanied by a decrease of the peak intensities of MoO^+ ((92 to 100 amu) + 16 amu (oxygen))

- Up to 150°C, significant changes in the relative intensities, but no further changes at temperatures higher than 300°C, i.e., sulfurization is finished

Study of the H/D exchange kinetics of ethylidyne ($\equiv\text{CCH}_3$) on Pt(111) single crystals (L2, p. 93), → Fig. 6.9

- Ethene was loaded at 200 K on a Pt(111) single crystal and, subsequently, evacuated at 400 K as well as exchanged with D_2 at this temperature
- Under these conditions, ethylidyne is formed on the platinum surface
- SIMS measurements performed with Ar^+ ions and a beam strength of 7 nA/cm²
- Sputtering of ca. 10 % of the material during the investigation
- CH_3 fragmentes cause a SIMS signal at 15 amu
- With each H/D exchange, the signal is shifted by 1 amu (CH_2D : 16 amu etc.)
- Curves in Fig. 6.9 show the time dependence of the SIMS signals of CH_3 (a), CH_2D (b), CHD_2 (c), and CD_3 (d)
- Simulation gives a rate constant of the H/D exchange at 400 K of $k = 1.15 \text{ s}^{-1}$

6.3 Secondary neutral mass spectrometry (SNMS)

6.3.1 Basics and experimental technique of SNMS

General remarks (L2, p. 95):

- More than 90% of the sputtered fragments of metals are neutrals
- Secondary neutrals are ionized after their sputtering, e.g. in a plasma or by means of an UV Laser beam, before they enter the mass spectrometer
- SNMS intensities do not depend on matrix effects (type of the chemical bonding of the sputtered atoms in the solid) and ionization potential
- Therefore, SNMS is more quantitative than SIMS

Quantitative description of the SNMS intensities:

- Signal intensities I_s^0 of the secondary neutrals at the detector are given by:

$$I_s = I_p \cdot Y \cdot c_{\text{surf}} \cdot \eta$$

with the primary ion density I_p , the sputter yield Y , surface concentration c_{surf} , and the equipment factor η , which corresponds to the transmission of the mass spectrometer

- In this case, the ionization probability, having a value of $\leq 1\%$ for the secondary ions, can be neglected
- Also ionic solids produce enough neutrals and allow the application of the above-mentioned equation
- Typically, the detection limit is in the ppm region

6.3.2 Application of SNMS

SNMS studies of the chemical composition of a Fe-Ni alloy in comparison with SIMS investigations (L2, p. 96): → Fig. 6.10

- Comparison of the SNMS and SIMS data shows significant differences in their sensitivities
- Real concentrations are obtained more by SNMS than by SIMS

6.4 Rutherford backscattering (RBS)

6.4.1 Basics and experimental technique of Rutherford backscattering

General remarks (L2, p. 97): → Fig. 6.11

- Ions with a high primary energy E_i are scattered at the atoms of solid surfaces
- The final energy E_f of the scattered ions depends on the following parameters

$$E_f = E_i \left(\frac{(M^2 - M_{ion}^2 \sin^2 \Theta)^{1/2} + M_{ion} \cos \Theta}{M + M_{ion}} \right)^2$$

with the kinetic energy E_i and mass M_{ion} of the incident ions, the mass M of the scattering atoms, and the scattering angle Θ

- The ratio E_f/E_i is assigned kinematic factor
- For scattering angles of 150 to 180°, the value of E_f/E_i is very different for different atoms acting as scattering sites, which allows the distinction of the sites: → Fig. 6.12
- For RBS, mono-energetic ions with relative high energies of 2 to 4 MeV are used, e.g., He^+ and Ne^+ ions

- Scattering occurs in a layer with a thickness of some μm
- For energies higher than 1 MeV, only weak sputtering occurs: → Fig. 6.4, left
- In the energy plot can be distinguished, whether ions are: → Fig. 6.13
 - directly scattered at the surface
 - penetrated deeply into a single crystal (channeling)
 - scattered at randomly oriented crystals (continuum edge)
 - scattered at heavy atoms on the surface
- In Fig. 6.13, the peak energy (top) or edge energy (middle) corresponds to E_f
- The integral or amplitude of the scattering peak depends on the scattering cross section

$$\sigma = \frac{Z_{\text{He}}^2 Z^2 e^4}{4E_i^2 \sin^4 \frac{\Theta}{2}}$$

with the atom number Z (to the power of 2) of the scattering atom and Z_{He} of the He^+ ions, the elementary charge e , the kinetic energy E_i of the incident He^+ ions, and the scattering angle Θ

6.4.2 Application of Rutherford backscattering

RBS study of the sulfurization of $\text{MoO}_3/\text{SiO}_2/\text{Si}(100)$ catalysts (L2, p. 101): → Fig. 6.14

- Preparation of the samples like in Section 6.2.2
- Signal assignment via Fig. 6.12 must be performed assuming a scattering angle of 170° ($80^\circ + 90^\circ$ according to Fig. 6.11)
- Peak at 3.4 MeV in Fig. 6.14 corresponds to a kinematic factor $E_f/E_i = 0.85$ ($3.4 \text{ MeV} / 4.0 \text{ MeV}$, He^+ have $E_{\text{kin}} = 4.0 \text{ MeV}$) and is due to molybdenum
- Peak at ca. 2.5 MeV in Fig. 6.14 corresponds to a kinematic factor $E_f/E_i = 0.62$ ($2.5 \text{ MeV} / 4.0 \text{ MeV}$) and indicates the incorporation of sulfur
- The continuum edge of ^{28}Si appears at 2.3 MeV ($E_f/E_i = 0.575$)
- The results of RBS show that the incorporation of sulfur into the catalysts is finished at 300°C

6.5 Low energy ion scattering (LEIS)

6.5.1 Basics and experimental technique of low energy ion scattering

General remarks (L2, p. 102):

- Also called ion scattering spectroscopy (ISS)
- Since scattering in the case of LEIS occurs exclusively at atoms of the outer surface, it is much more surface sensitive in comparison with RBS (RBS has larger penetration depth of some μm)
- Incident noble gas ions have energy of 0.1 to 4 keV and low beam densities
- Scattering process is described in Fig. 6.11
- Primary ions penetrating into the sample material are immediately neutralized and can not be detected
- Low-energetic primary ions are scattered at the electrostatic field of the scattering nuclei
- LEIS depends on the electrostatic potential $V(r)$ of the scattering sites

$$V(r) = \frac{Z_{\text{ion}} e Z e}{r} \cdot \frac{0,885 a_0}{2r(\sqrt{Z_{\text{ion}}} + \sqrt{Z})^{2/3}}$$

with the atom number Z_{ion} of the ions and Z of the scattering site, the elementary charge e , the lattice constant a_0 , and the distance r

- The first term corresponds to the Coulomb potential, while the second term is a shielding function
- Due to the shielding of the nuclear Coulomb potential by the electrons of the corresponding nucleus, LEIS depends less on the atom number Z (linear only) of the scattering atoms in comparison with RBS

6.5.2 Application of low energy ion scattering

LEIS studies on Cu/Al₂O₃ catalysts (L2, p. 105): → Fig. 6.15

- Al₂O₃ was impregnated with a solution of copper salt and, subsequently, calcined
- The LEIS spectrum was obtained with He⁺ ions of an energy of 3 keV
- The spectrum shows signals of the main components Cu, Al, and O and, in addition, also a signal of fluorine impurities occurs

- The latter finding demonstrates the high sensitivity of LEIS for light atoms, such as fluorine, as scattering sites
- The very left peaks are due to sputtered atoms
- This peak starts at 40 eV, which indicates a positive charging of the sample material
- Exact determination of the kinematic factor E_f/E_i requires, therefore, a charge shift correction

7. Vibrational spectroscopy

7.1 Basics of vibrational spectroscopy

Distinction of 4 methods:

- Infrared spectroscopy (IR or FTIR)
- Raman spectroscopy
- Electron energy loss spectroscopy (EELS)
- Inelastic neutron scattering (INS, Section 3.3.3)

Description of molecular vibrations by a harmonic oscillator (L2, p. 194)

- In the case of two-atomic molecules and small deviations from the equilibrium distance, the potential $V(r)$ of the harmonic oscillator can be used:

$$V(r) = \frac{1}{2} k (r - r_{\text{eq}})^2$$

with the atom-atom distance r of the vibrating atoms, their equilibrium distance r_{eq} , and the force constant k of the vibrating bond

- The vibration energy levels E_n are equidistant:

$$E_n = (n + \frac{1}{2}) \hbar \nu$$

with the integer number n of the energy levels, the Planck constant \hbar , and the vibration frequency ν

$$\nu = \frac{1}{2\pi} \sqrt{\frac{k}{\mu}}$$

which includes the reduced mass μ

$$\mu = \frac{m_1 m_2}{m_1 + m_2}$$

with the masses m_1 and m_2 of the vibrating atoms

Description of molecular vibrations by the Morse function (L2, p. 196)

- For large deviations from the equilibrium distance of the vibrating atoms, the potential $V(r)$ is described by the Morse potential

$$V(r) = D (1 - e^{-a(r-r_{eq})})^2$$

with the dissociation energy D of the vibrating bond and the slope a of the function

- For a comparison of the above-mentioned potentials, see Fig. 7.1

Classification of the vibrational spectroscopy: → Fig. 7.2

- Vibration frequencies of ca. 10^{11} to 10^{16} s⁻¹ with energies of ca. 0.001 to 5 eV
- The vibration energies are significantly lower in comparison with the energies of X-ray scattering and significantly higher than the electron transitions in ESR spectroscopy

Different types of vibrations: → Fig. 7.3

- Stretching vibrations with symbol ν
- Bending vibrations in an atom layer with the symbols δ and β for scissor and rocking vibrations, respectively
- Bending vibrations out of the atom layer with the symbols γ and ρ , mostly for large molecules with different wagging and twisting vibrations, respectively
- For a survey on the abbreviations of the different vibration types, see Tab. 7.1

7.2 Infrared spectroscopy (IR)

7.2.1 Basics and experimental technique of IR spectroscopy

General remarks (L4, p. 1):

- Distinction of the far, middle (mid), and near infrared (NIR) regions: → Tab. 7.2
- The NIR region overlaps with the region of electron transitions (e.g. UV/Vis)
- IR spectra are mostly plotted as a functions of the wavenumber $\tilde{\nu}$, i.e. in cm⁻¹
- The relationship to the wavelength λ is given by:

$$\tilde{\nu} \text{ (cm}^{-1}\text{)} = 10^4 / \lambda \text{ (\mu m)} \quad \text{or} \quad \lambda \text{ (\mu m)} = 10^4 / \tilde{\nu} \text{ (cm}^{-1}\text{)}$$

- There are characteristic vibration regions for O-H, N-H, C-H, C=C, C-O, and Si-O bonds: → Tab. 7.3
- Allows investigations of the framework of solid catalysts and their surface sites as well as of adsorbates at the catalyst surface (reactants, intermediates etc.)

Survey on the experimental techniques of IR spectroscopy (L4, p. 44): → Tab. 7.4

a) Transmission technique

- Study of the lattice vibrations in the region of 300 to 1250 cm^{-1}
 - samples have contact to air during the IR measurement
 - powder samples are mixed with KBr or CsI and pressed to a wafer having a thickness of ca. 3 mm
- Investigation of solid catalysts in the region of 2200 to 7500 cm^{-1}
 - samples are pressed to self-supporting wafers with an areal density of ca. 10 mg/cm^2

b) Technique of diffuse reflection

- Study of activated powder samples in the region of 2200 to 7500 cm^{-1}
- Reflection of IR radiation on the surface of a loose powder bed
- Used in the case of bad transmission properties of the sample under study or in the case that samples can not be pressed to self-supporting wafers

c) Technique of reflection-absorption

- In the case of reflection-absorption infrared spectroscopy (RAIS), the IR beam is irradiated in a very small angle, i.e., nearly parallel to the surface of the solid
- Excitation of vibrations in molecular bonds with dipole moments, which are perpendicularly arranged to the surface of the solid
- Often used for the study of adsorbate complexes on the surface of single crystals
- This technique is also utilized by EELS (electron energy loss spectroscopy), however, by irradiation of electron beams (corresponding to electron waves): → Section 7.4

d) Emission spectroscopy

- Study of metal samples at very high temperatures
- Similar to the determination of the temperature in commercial applications via Wien's shift law (NIR region)

Technique of IR spectrometers (L4, p. 41): → Fig. 7.4

- Nowadays, Fourier transform (FT) IR spectrometers are used and the earlier dispersive IR spectrometers with an optical prism or lattice disappear more and more
- FTIR spectrometers consist of an interferometer with a fixed mirror M1 and a mobile mirror M2, which changes the x -position in a well-defined manner during the measurement
- The detector records an interferogram $G(x)$, which depends on the x -position of mirror M2
- The interferogram contains the information on the energy density for all wavelengths of the polychromatic IR beam used for exciting the vibrations
- Finally, the function $G(x)$ is Fourier transformed into the frequency space $F(\nu)$ or $F(\tilde{\nu})$
- While dispersive IR spectrometers needed ca. 20 minutes for the recording of one spectrum, the FTIR spectrometer records a spectrum in ms to few s
- The FTIR technique allows rapid scanning and rapid accumulation of spectra

Experimental technique of FTIR transmission spectroscopy (L4, p. 42)

- IR cell suitable for the activation and study of thin sample wafers (ca. 10 mg/cm^2) in vacuum outside of the IR beam: → Fig. 7.5
- Magnetically coupled lift for the transportation of the activated sample wafer into the IR beam
- Replacement of the sample wafers on top of the cell
- Cell is suitable for in situ FTIR investigations, i.e., in a temperature range up to 873 K; use of isolated IR windows: → Fig. 7.6
- Allows experiments under continuous flow conditions like in fixed-bed reactors
- Suitable for the combination of FTIR spectroscopy and temperature-programmed reduction (TPR), oxidation (TPO), and desorption (TPD) of probe molecules
- Available spectral range depends on the IR windows: → Tab. 7.5
- CaF_2 is the mostly used window material (ca. 200 EUR per window)

Experimental technique of DRIFT spectroscopy (L2, p. 200; L4, p. 42)

- Diffuse reflectance infrared Fourier transform (DRIFT) spectroscopy

- The IR radiation is diffusely reflected from the sample surface and must be collected in front of the detector
- Collection of diffuse IR radiation via optical lenses (not often): → Fig. 7.7
- More often, an integration sphere is used for collecting the diffuse IR radiation at the inner surface and reflection of this collected radiation to the detector: → Fig. 7.8
- This system has a higher efficiency in comparison with optical lenses
- Sample holder of the DRIFT cell can be used for in situ studies; in this case, a sample heater and an exhaust gas supply system is installed: → Fig. 7.9
- Plotting of DRIFT spectra via the Kubelka-Munk function $F(R_\infty)$

$$F(R_\infty) = (1 - R_\infty)^2 / 2 R_\infty$$

with the reflectance R_∞ (intensity of the reflected beam) of a sample with infinite thickness

- By the DRIFT spectrometer, R_∞ is measured in the whole spectral range and, subsequently, $F(R_\infty)$ is calculated point by point before plotting

Experimental technique of attenuated total reflection (ATR) spectroscopy (L6, p. 227): → Fig. 7.10

- Basic principle is the multiple total reflection of the IR beam in a single crystal (IRE: internal refractive element) made by Ge, ZnSe, GeAsSe or similar materials, which acts as light conductor and has contact to the sample material under study
- The component of the electromagnetic field of the incident IR beam, which is perpendicular to the axis of the ATR crystal, causes a 'evanescent' (exponentially decreasing) wave penetrating with the depth d_p into the sample

$$d_p = \lambda / 2\pi \sqrt{n_1^2 \sin^2 \Theta - n_2^2}$$

with the wavelength λ of the incident IR beam, the refraction index n_1 of the ATR crystal, the refraction index n_2 of the sample, and the angle Θ of the incident IR beam

- The effective penetration depth d_e depends of the number N_i of the total reflections

$$d_e = \sum_i N_i d_p i$$

- For an IRE made by Ge with $n_1 = 4$ in contact with an aqueous sample with $n_2 = 1.33$ and $\Theta = 45^\circ$, the penetration depth is 0.22 to 0.44 μm in dependence on the orientation of polarization plane and the wavelength of the incident IR beam
- In the case of the installation of an IRE for ATR studies as well as of IR windows for FTIR studies in a reactor, the composition of a fluid phase and; simultaneously, the molecules adsorbed on a solid catalyst can be investigated: → Figs. 7.11 and 7.12

Quantitative studies via FTIR spectroscopy (L4, p. 35)

- Exclusively possible for transmission mode measurements
- Application of the Lambert-Beer equation

$$\ln\left(\frac{I}{I_0}\right) = -\varepsilon C_{\text{as}} d$$

with the intensity I_0 of the incident IR beam, the intensity I measured after transmitting the sample material, the molar extinction coefficient ε , the number C_{as} of the absorbing species, and the thickness d of the sample (way of the IR beam through the sample)

- In literature, the extinction coefficients ε of a number of surface species and adsorbate complexes are given (L4, p.38): → Tab. 7.6
- However, these values can strongly vary for different authors (see, e.g., ε values of OH stretching vibrations of H-Y zeolites)
- For the study of surface sites, therefore, combination of FTIR spectroscopy with quantitative adsorption of probe molecules is very useful: → Section 7.2.2

7.2.2 Application of IR spectroscopy

FTIR studies of the lattice vibrations of crystalline aluminosilicates (L4, p. 49)

- Measurements were performed in transmission mode with KBr or CsI wafers
- Investigation of (i) intra-tetrahedral and (ii) inter-tetrahedral vibrations: → Fig. 7.13
 - (i): antisymmetric and symmetric stretching and bending vibrations of the TO_4 units
 - (ii): antisymmetric (1050 to 1150 cm^{-1}) and symmetric (750 to

820 cm⁻¹) stretching vibrations (ii) between TO₄ units as well as double ring (500 to 650 cm⁻¹) and ring opening vibrations (300 to 420 cm⁻¹)

- Exclusively the inter-tetrahedral vibrations are sensitive for the structure
- In the case of faujasites (zeolites LSX, X, Y, USY), the positions of the antisymmetric (σ_1 , $\tilde{\nu}_{as}$) and symmetric (σ_2 , $\tilde{\nu}_s$) stretching vibrations correlate with the aluminum content of the lattice: → Figs. 7.14 and 7.15
- The number N_{Al} of aluminum atoms per unit cell (uc) can be calculated via (J.R. Sohn et al., *Zeolites* 6 (1986) 225):

$$N_{Al} [\text{uc}] = 0.776 (1086 - \tilde{\nu}_{as} [\text{cm}^{-1}])$$

$$N_{Al} [\text{uc}] = 1.007 (838 - \tilde{\nu}_s [\text{cm}^{-1}])$$

FTIR studies of the different types of surface OH groups on crystalline aluminosilicates (L4, p. 74)

- Measurements are performed in the transmission mode with thin self-supporting wafers consisting of the activated sample material
- Study of bridging OH groups (SiOHAl) existing in the different structure units and cages of the above-mentioned materials: → Fig. 7.16
- There are 6 different vibration types in the local structure of bridging OH groups: → Fig. 7.17
- The most important vibration type is the stretching vibration $\tilde{\nu}_{OH}$: → Fig. 7.18:
 - SiOH band at ca. 3740 cm⁻¹: OH groups at surface defects
 - HF band, ca. 3610 - 3650 cm⁻¹: SiOHAl groups in large structure units and pores
 - LF band, ca. 3520 - 3550 cm⁻¹: SiOHAl groups in small cages and pores
- OH groups in small structure units and are involved in additional electrostatic interactions leading to a decrease of their vibration frequency (LF band: low-frequency band), in contrast to OH groups in large cages without additional interactions (HF band: high-frequency band)
- The different vibrations in the local structure of OH groups cause bands of combination vibrations in the IR and NIR regions (K. Beck et al., *Microporous Mater.* 2 (1993) 1): → Tab. 7.7

- In the case of H-Y zeolites, e.g., combination vibrations of OH stretching vibrations $\tilde{\nu}_{OH}$ and OH bending vibrations δ occur and can be detected: →

Fig. 7.19

- LF band: $3548 \text{ cm}^{-1} + 1057 \text{ cm}^{-1} = 4605 \text{ cm}^{-1}$
- HF band: $3640 \text{ cm}^{-1} + 1028 \text{ cm}^{-1} = 4668 \text{ cm}^{-1}$

- The specific wavenumbers $\tilde{\nu}_{OH}$ of the OH stretching vibrations depend on the aluminum content of the zeolite lattice,
- The aluminum content affects the mean electronegativity S^m of the zeolite lattice (see Section 5.2.2), which correlates with $\tilde{\nu}_{OH}$: → Fig. 7.20
- FTIR studies of the thermal stability of SiOHAl groups in zeolites are often performed in a semi-quantitative manner, i.e., plotting of the band integral or band amplitude as a function of the calcination temperature: → Fig. 7.21

Characterization of the chemical properties of surface OH groups in crystalline aluminosilicates via probe molecules (L4, p. 106 and 131)

- Use of pyridine as probe molecule for studying the type (Brønsted or Lewis) acid sites and their location
- Two characteristic bands of pyridine are evaluated: → Fig. 7.22, left
 - ca. 1540 cm^{-1} : pyridinium ions at Brønsted acid sites
 - ca. 1445 cm^{-1} : pyridine coordinated to Lewis acid sites
- FTIR spectroscopy of calcined zeolites upon adsorption of pyridine allows the investigation of the temperature dependence of acid sites: → Fig. 7.22, right
- Suitable way for the quantification of IR bands caused by acid sites, without to use an extinction coefficient, is the stepwise adsorption, e.g., of pyridine and simultaneous FTIR spectroscopy: → Fig. 7.23
- Study of the acid strength of surface OH groups requires probe molecules with low basicity (pyridine is often totally protonated by acidic catalysts and not useful in this case)
- These weakly basic probe molecules should interact with the surface OH groups under study via hydrogen bonds causing a band shift, which can be correlated with the acid strength: → Fig. 7.24
- Frequency shifts $\Delta\tilde{\nu}_{OH}$ of the OH stretching vibrations upon adsorption of CO (measurements must be performed at $T = 120 \text{ K}$):

| | |
|--|--------------------------|
| • SiOH groups | ca. 90 cm^{-1} |
| • AlOH groups at extra-framework aluminum | 140-195 cm^{-1} |
| • POH groups in AlPO ₄ and SAPO | 175-195 cm^{-1} |
| • SiOHAl groups in SAPO | 254-280 cm^{-1} |
| • SiOHAl groups in H-Y zeolites | ca. 290 cm^{-1} |
| • SiOHAl groups in H-ZSM-5 zeolites | ca. 310 cm^{-1} |

ATR studies on the oxidation of ethanol on a 5%Pd/TiO₂ catalyst (L6, p. 253), → Fig. 7.25

- Application of an ATR cell like shown in Figs. 7.11 and 7.12
- IRE crystal was made by ZnSe
- Measurements at 298 K under continuous-flow conditions with H₂- (up to $t = 75$ s) and O₂-saturated ethanol (starting at $t = 355$ s)
- Recording of the ATR IR spectra (Fig. 7.25, left) at the times assigned by 1 to 6: → Fig. 7.25, right
 - band at 1300 cm^{-1} indicates the changes of the catalyst
 - band at 1402 cm^{-1} stands for the formation of acetates on the catalyst
 - band at 1765 cm^{-1} hints to carbonyl groups
 - band at 1840 cm^{-1} is due to CO adsorbed on the catalyst

7.3 Raman spectroscopy

7.3.1 Basics and experimental technique of Raman spectroscopy

General remarks (L2, p. 208; L5, p. 62):

- Simply, the Raman effect can be considered as an inelastic scattering of photons, which leads to a loss of a small amount of energy used for exciting vibrations
- In contrast to IR spectroscopy, which is an one-photon excitation process, the Raman effect is a two-photon excitation process
- At first, a photon with frequency ν_0 excites a vibration; subsequently, another photon is emitted with the energy ($h[\nu_0 \pm \nu]$)

- Raman spectroscopy can be applied for species, which are characterized by a molecular polarizability $\alpha(t)$
- In this case, the induced dipole moment $\mu(t)$ is given by

$$\mu(t) = \alpha(t) E(t)$$

with the polarizability $\alpha(t)$ and the electric field $E(t)$ of the incident beam

- The vibration of the excited molecule leads to a time dependent polarizability:

$$\alpha(t) = \alpha_0 + \alpha \cos(2\pi \nu_i t + \phi)$$

with the vibration frequency ν_i and the phase angle ϕ

- In this case, the induced dipole moment $\mu(t)$ is given by:

$$\mu(t) = \alpha(t) E(t) = [\alpha_0 + \alpha \cos(2\pi \nu_i t + \phi)] E_0 \cos(2\pi \nu_0 t)$$

or

$$\mu(t) = \alpha_0 E_0 \cos(2\pi \nu_0 t) + (\alpha/2) E_0 \cos[2\pi (\nu_0 - \nu_i) t + \phi] + (\alpha/2) E_0 \cos[2\pi (\nu_0 + \nu_i) t + \phi]$$

with the electric field E_0 and the excitation frequency ν_0

- Therefore, 3 bands occur in the Raman spectrum at frequencies of: → Fig.7.26

- ν_0 Rayleigh band
- $\nu_0 - \nu_i$ Stokes band
- $\nu_0 + \nu_i$ anti-Stokes band

- The intensity of the anti-Stokes band is always much weaker in comparison with the Stokes band since the content of molecules excited with a higher frequency is smaller
- In the Raman spectrum, the frequency difference $\Delta\nu = \nu_0 - \nu_i$ to the frequency of the exciting Laser (ν_0) is plotted
- Advantages of Raman spectroscopy in comparison with IR spectroscopy:
 - excitation can be performed in the UV to IR region
 - therefore, Raman cells can have relatively cheap quartz glass windows
 - no problems with water bands since measurements can be performed in the UV region
 - the gas phase does not contribute to the spectrum, i.e., exclusively excitation of vibrations of compounds in or on the solid materials

- under study
- use of excitation Lasers allows a high spatial resolution (Raman microscopy) and the study of very small samples (picogram region)
 - Disadvantages of Raman spectroscopy in comparison with IR spectroscopy:
 - lower intensities (lower sensitivity) of Raman bands
 - lower spectral resolution
 - higher costs
 - heating of the sample by the irradiating Laser
 - fluorescence of the sample material can lead to strong background radiation; therefore, use of pulsed Lasers and triggered detectors since fluorescence is a retarded process (10^{-6} s)

Experimental technique of Raman spectroscopy (L5, p. 59), → Fig. 7.27

- Excitation is mostly performed with Nd-YAG (532 nm), He/Ne (633 nm), Ar⁺ (351 to 514 nm) or Kr⁺ Lasers (337 to 676 nm) with a power of 10 to 500 mW
- In front of the monochromator, often a Rayleigh filter is installed for blocking the ν_0 frequency
- This filter can be also an edge filter, which cuts all frequencies higher than a limiting frequency, i.e., also the anti-Stokes bands are suppressed
- Detectors are photomultiplier or CCD (charge-coupled device) detectors
- In situ Raman cells reach temperatures until 1773 K and pressures of ca. 10 bar
- Raman cells contain often a rotating sample holder (A), a rotating mirror system for the Laser beam (B) or a lenses system causing a widening of the Laser beam (C) in order to decrease the local heating of the sample material: → Fig. 7.28
- The construction of the cell can be different concerning the path of the Laser beam, the heating system, and the flow routes of reactants (L5, p. 70): → Fig. 7.29

7.3.2 Application of Raman spectroscopy

Raman studies of the lattice vibrations of faujasite-type zeolites (L4, p. 58)

- Excitation with a Nd-YAG Laser with a power of 450 mW
- Samples have same structure type, but different aluminum contents in the lattice
- In the FTIR spectrum shown in Fig. 7.14, strong bands of antisymmetric (σ_1) and symmetric (σ_2) stretching vibrations occur at 1100 and 800 cm^{-1} (sensitive for the $n_{\text{Si}}/n_{\text{Al}}$ ratio)
- In the Raman spectrum, the σ_1 and σ_2 bands are very weak, but contain the same information like in the FTIR spectra: → Fig. 7.30

Raman studies of the formation of supported MoO_3 catalysts (L2, p. 210)

- The supports Al_2O_3 and SiO_2 were impregnated with ammoniumhepta-molybdate $((\text{NH}_4)_6\text{Mo}_7\text{O}_{24} \cdot 4 \text{ H}_2\text{O})$ in water at different pH values (wet samples) and calcined at 775 K in air
- The spectra show strongly different band intensities for the sample prepared at different pH values: → Fig. 7.31, top
- The table gives the assignment of the bands of the different stretching vibrations (ν , ν_s , ν_{as}) and bending vibrations (δ): → Fig. 7.31, bottom
- The pH value determines, what kind of molybdenum complex exist on the wet SiO_2 :
 - $\text{Mo}_8\text{O}_{26}^{4-}$ at $\text{pH} < 4$
 - $(\text{NH}_4)_6\text{Mo}_7\text{O}_{24} \cdot 4 \text{ H}_2\text{O}$ at $\text{pH} = 4.8-6.8$
 - also MoO_4^{2-} at $\text{pH} > 8$
- After calcination of the $\text{MoO}_3/\text{SiO}_2$ material, bands of a crystalline MoO_3 phase (ca. 816 cm^{-1}) dominate the spectra
- In contrast, the MoO_3 components on Al_2O_3 are strongly bound to the support and form polymolybdates (broad bands at 852 to 958 cm^{-1})

In situ Raman studies of Al_2O_3 - and SiO_2 -supported V_2O_5 catalysts (G. Garcia et al., Catal. Today 78 (2003) 219)

- Impregnation of the supports with ammoniummetavanadate according to 4 vanadium atoms per nm^2 (16 wt.-%)
- Co-impregnation with potassiumhydroxide up to maximum 6 wt.-% potassium
- Calcination of the samples at 573 K in O_2/He for 1 h

- Spectra were recorded using an Ar⁺ Laser with the wavelength of 514 nm
- The Raman spectra of the V₂O₅/x%K/Al₂O₃ samples show stretching vibration bands at 1027 cm⁻¹ due to terminal V=O species located at the catalyst surface: → Fig. 7.32
- With increasing potassium contents, the band at 1027 cm⁻¹ is shifted to lower wavenumbers (up to 988 cm⁻¹ for 6 wt.-% K), which indicates a weakening of the terminal V=O bonds by the incorporation of potassium
- For the V₂O₅/SiO₂ material with 2 wt.-% V₂O₅, the stretching vibration band of terminal V=¹⁶O bonds occurs at 1031 cm⁻¹ and of terminal V=¹⁸O bonds at 988 cm⁻¹: → Fig. 7.33 (0 sec)
- After starting the ethane oxidation in the presence of ¹⁶O₂ gas, the band of V=¹⁸O bonds at 988 cm⁻¹ strongly decreases
- ¹⁸O is consumed by the oxidation reaction and is replaced by ¹⁶O, which contributes to the band at 1031 cm⁻¹

7.4 Electron energy loss spectroscopy (EELS)

7.4.1 Basics and experimental technique of EELS

General remarks (L2, p. 213):

- Excitation of vibrations by irradiation of monochromatic electrons with very low energy (ca. 1 to 10 eV)
- Especially, lattice vibrations in the surface region of solids and vibrations of adsorbed molecules are excited
- The energy E of the scattered low energy electrons is measured:

$$E = E_p - h \nu \quad \text{or} \quad h \nu = E_p - E \quad (\text{plot of the spectrum})$$
 with the energy E_p of the primary electrons (irradiated electrons) and the frequency ν of the excited vibration
- While IR and Raman spectroscopy are limited to compounds with permanent dipole moment and molecular polarizability, respectively, EELS is able to excite and detect all kind of vibrations
- Distinction of: → Fig. 7.34
 - dipole scattering: Utilizes the wave character of the electron beam; the component of the electromagnetic field being perpendicular to the solid surface excites the ν_1 vibrations

- impact scattering: Short-range interactions (collisions) of the electrons acting as particles with adsorbate molecules causes the excitation of vibrations (ν_1 und ν_2) in a large angle range
- The EELS equipment consists of an electron source (filament), a monochromator, an analyzer for the stepwise reading of electron with different energies and a counter tube: → Fig. 7.35

7.4.2 Application of EELS

EELS studies on the chemisorption of CO on nickel single crystals (W. Ho, *J. Phys. Chem.* 91 (1987) 766): → Fig. 7.36

- In the above described EELS equipment, electrons with an energy of $E_p = 3$ eV were irradiated in an angle of 50° to nickel single crystals
- The CO coverage Θ of the surface was ca. 0.2 (low) and 0.5
- In the EELS spectra, C-O and M-CO bands due to 1- and 2-dentate chemisorption of CO occur: → Fig. 7.36, top and bottom
- For Ni(111), the 2-dentate chemisorption of CO dominates in the spectra, while for the other surfaces, there is a mixing of chemisorption states of CO

8. UV/Vis and EPR spectroscopy

8.1 Comparison of both methods

Joint properties:

- Both methods study and utilize electron transitions

Differences:

- UV/Vis spectroscopy studies electron transitions from a low level to an excited level without changing the electron spins
- EPR spectroscopy studies changes of the electron spins

8.2 UV/Vis spectroscopy

8.2.1 Basics and experimental technique of UV/Vis spectroscopy

General remarks (L7, p. 1039):

- Ultraviolet and visible spectroscopy (UV/Vis)
- Electron transitions and transitions of charge densities occurring between different orbitals or levels of the same atoms (e.g. metal) or with neighbouring atoms (e.g. metal or ligand)

Distinction of the following excitations (L7, p. 1040):

- Metal-centered (MC) transitions
 - $d \rightarrow d$ and $(n-1)d \rightarrow ns$ in transition elements
 - $f \rightarrow f$ and $4f \rightarrow 5d$ in rare earth elements
 - $ns \rightarrow np$ in main group elements
- Charge-transfer (CT) transitions
 - metal-to-metal charge transfer (MMCT), also called intervalence transitions (e.g. $Fe^{2+} \rightarrow Fe^{3+}$ in Fe_3O_4 or Fe^{2+} to Ti^{4+} in sapphire)
 - ligand-to-metal (LMCT) and metal-to-ligand charge transfer (MLCT)
 - transitions between molecular levels ($\sigma \rightarrow \sigma^*$, $n \rightarrow \sigma^*$, $n \rightarrow \pi^*$, $\pi \rightarrow \pi^*$) in inorganic and organic molecules or ions, which are free or coordinated to metals, also called ligand-centered (LC) transitions

There are various assignments for transitions (L4, p. 347): → Tab. 8.1

- The above-mentioned assignments were introduced by Kasha
- In addition, assignments by Mulliken and on the base of the group theory exist

Characteristic spectral regions of the above-mentioned electron transitions (L7, p. 1041; L4, p. 346): → Figs. 8.1 and 8.2

- The low-energetic d-d and MMCT transitions cover a range up to the NIR region
- An overlap with combination vibration bands is possible (see Section 7.2.2)

- Transitions between molecular orbitals occur in the region of about 200 to 750 nm

Experimental technique (L4, p. 366):

- Dispersive spectrometers are dominating since UV/Vis bands are often very broad and high resolution is not required
- Often, commercial laboratory UV/Vis spectrometers work in the transmission mode as double-beam equipments with different beam lines for the sample and the reference material
- Application of photomultiplier detectors or diode array detectors: → Figs. 8.3 and 8.4
- Diode array detectors allow the simultaneous recording of the whole spectral range
- Deuterium/halogen lamps are often used as UV/Vis source in the region of 215 to 2500 nm

Cells used for in situ UV/Vis spectroscopy under reaction conditions (B.M.

Weckhuysen, *Phys. Chem. Chem. Phys.* 5 (2003) 4351): → Figs. 8.5 and 8.6

- The Praying-Mantis cell is used in commercial laboratory UV/Vis spectrometers for measurements in the diffuse reflection mode (like DRIFT)
- Allows measurements in the region of 200 to 800 nm and at temperatures up to 823 K under flow conditions
- Recording time of a single spectrum of 0.028 s possible, i.e., observation of rapid processes is possible
- Because of their high sensitivity, UV/Vis spectrometers can be equipped with glass-fiber optics
- A glass-fiber optics can be installed in standard fixed-bed reactors suitable for catalytic studies under flow conditions
- In this case, the measurements are performed in the diffuse reflection mode and the reference material is recorded and stored before studying the samples

Evaluation of the UV/Vis spectra:

- In the transmission mode, the spectral absorption as a function of the wavelength is plotted

- The x-axis corresponds to the wavelength λ in nm or the wavenumber $\tilde{\nu}$ in cm^{-1} (see Section 7.2.1)
- In the case of measurements in the diffuse reflection mode, the evaluation of the spectral absorption is performed according to Kubelka-Munk (see Section 7.2.1)
- In the case of measurements in the transmission mode, the quantitative evaluation of the absorption is made according to Lambert-Beer (see Section 7.2.1)

8.2.2 Application of UV/Vis spectroscopy

UV/Vis studies of the distribution of cobalt cations in the SCR (selective catalytic reduction) catalyst Co-FER (P. Ciambelli et al., *Topics in Catalysis* 42-43 (2007) 177):

- Zeolite ferrierite (FER) has a structure with one-dimensional 10-ring pores, which are connected via 8-ring windows
- There are 4 crystallographically non-equivalent extra-framework cation positions (B, C, F, G): → Fig. 8.7
- Cobalt cations in ferrierite can act as catalytically active sites in the conversion of NO and NO_2 in N_2 , H_2O , and CO_2 in the presence of CH_4
- The UV/Vis measurements were performed in the diffuse reflection mode on a Lambda 40 Perkin-Elmer spectrometer in the spectral range of 350 to 900 nm
- The UV/Vis spectrum of Co-FER shows 3 bands due to metal-centered d-d transitions of the cobalt cations (Co1b, Co1a, Co2a): → Fig. 8.8
- The observed bands have the following assignments:
 - Co1b: position C, 448 to 465 nm or 21500 to 22320 cm^{-1}
 - Co1a: position G, 521 to 549 nm or 18200 to 19200 cm^{-1}
 - Co2a: position B, 637 to 661 nm or 15100 to 15700 cm^{-1}
- The absorption coefficients are $0.5 \cdot 10^3 \text{ cm}^{-1}$, $1.2 \cdot 10^3 \text{ cm}^{-1}$, and $1.3 \cdot 10^3 \text{ cm}^{-1}$, respectively
- In the spectrum of the fresh catalyst, the band of cobalt cations on position C in 5-membered oxygen rings dominates the spectrum: → Fig. 8.8a

- In the spectrum recorded after performing the SCR reaction, the band of cobalt cations on position G in 6-membered oxygen rings dominates: → Fig. 8.8b
- Hence, the SCR reaction causes a redistribution of cobalt cations and their migration to larger oxygen rings

UV/Vis studies of the formation of nickel catalysts supported on SiO_2 (L7, p. 1045):

- Observation of the d-d transitions of Ni^{2+} cations after the loading of $\text{Ni}(\text{NH}_3)_6^{2+}$ on SiO_2 and subsequent drying and calcination
- Three different d-d transitions were observed with band positions depending on the type of the coordinating ligands: → Tab. 8.2
- A red shift (left shift) of the bands occurs after the calcination if the Ni^{2+} cations are more strongly coordinated to the support: → Fig. 8.9, left
- This finding can be explained by a stronger coordination of Ni^{2+} to SiO^- than with H_2O and NH_3 before the calcination: → Tab. 8.2 and Fig. 8.9
- The combination vibration region contains bands of SiOH groups and NH_3 ligands, which strongly decrease upon drying at 353 K and calcination (stronger Ni^{2+} /support interaction)

UV/Vis studies of the formation of carbenium ions during the alkylation of isobutane with butene on zeolite La,H-Y (I. Kiricsi et al., *Chem. Rev.* 99 (1999) 2085):

- A Lambda 9 Perkin-Elmer spectrometer with variable-temperature cell for studies in the diffuse reflection mode in the range of 190 to 1500 nm was used
- Observation of UV/Vis bands caused by carbenium ions, which are intermediates in the above-mentioned reaction and also responsible for the deactivation of the catalyst materials after long time-on-stream
- Following assignments of the bands were suggested:
 - monoenylic carbenium ions: 280 to 300 nm
 - dienylic carbenium ions: 360 to 380 nm
 - trienylic carbenium ions: 430 to 470 nm
- The above-mentioned carbenium ions can be observed after 1-butene/isobutane conversion on acidic zeolites at 523 to 773 K: → Fig. 8.10

- UV/Vis spectroscopy is the most sensitive method for studying carbenium ions on solid catalysts

UV/Vis studies of the coke formation on H-SAPO-34 catalysts during the conversion of methanol at 673 K (Y. Jiang et al., *Stud. Surf. Sci. Catal.* 170 (2007) 1137)

- Glass-fiber UV/Vis spectrometer Avantes HPSUV1000A, AvaLight-DH-S Deuterium light source, and fixed-bed reactor according to Fig. 8.6
- Measurements were performed under continuous flow conditions ($W/F_{\text{me}} = 25$ g/mol) with catalyst weight of 100 mg
- Study of bands in the region of 200 to 600 nm due to $\pi-\pi^*$ transitions caused by the formation of aromatics and carbenium ions (Fig. 8.11):
 - dienes: 245 nm
 - aromatics: 280 nm
 - di- and trienylic carbenium ions: 345 and 470 nm
 - polycyclic aromatics (coke): 400 nm
- With increasing reaction time, a structured band occurred at 385 to 425 nm, which was assigned to alkylated anthracenes (consisting of 3 aromatic rings)
- The above-mentioned coke compounds block the pores and are responsible for catalyst deactivation

8.3 EPR spectroscopy

8.3.1 Basics and experimental technique of EPR spectroscopy

General remarks (L8, p. 29):

- Electron paramagnetic resonance (EPR), electron spin resonance (ESR)
- Caused by the Zeeman interaction of the spins S of unpaired electrons in an external magnetic field
- Unpaired electrons have a spin $S = 1/2$ corresponding to the dipole moment μ_e

$$\mu_e = -\mu_B g_0 S = -\gamma_e \hbar S$$

with the g_0 factor of the free electrons, $g_0 = 2.002322$, the Bohr magneton $\mu_B = 9.27401 \times 10^{-24}$ J/T, and the gyromagnetic ratio $\gamma_e = \mu_B g_0$ of the electrons.

- The dipole moment μ_e interacts with the magnetic flux density B_0 of the external magnetic field leading to the energy

$$E = \mu_B g_0 m_S B_0$$

- The splitting of the energy levels ($\Delta m_s = 1$) due to the Zeeman interaction is

$$\Delta E = \mu_B g_0 B_0 = h \nu_0$$

- According to $\nu_0/B_0 = \frac{g_0 \mu_B}{h} = \gamma_e/2\pi = 28.0250 \text{ GHz/T}$,
a magnetic field of $B_0 = 1 \text{ T}$ leads to a resonance frequency of the electron spins of 28 GHz (Larmor frequency $\nu_0 = \omega_0/2\pi$) corresponding to a wavelength of ca. 1 cm, which is about three orders of magnitude higher than the Larmor frequency of ^1H nuclei in the same B_0 field (42.5670 MHz/T)

Shapes of EPR signals:

- The most important interaction of the electron spins S in magnetic B_0 fields is the Zeeman interaction

$$H_Z = \mu_B S \bar{g} B_0$$

with the anisotropic \bar{g} tensor

- In the common case, the \bar{g} tensor is described by the principle axis values g_1 , g_2 , and g_3 , which are responsible for the singularities of the EPR signals: → Fig. 8.12, right
- In the case of an axial symmetry, the EPR signals depend on the tensor components $g_{||} = g_1$ and $g_{\perp} = g_2 = g_3$: → Fig. 8.12, left
- For a cubic symmetry ($g_1 = g_2 = g_3$), the \bar{g} tensor is replaced by a g factor leading to a symmetric EPR signal

Hyperfine splitting of EPR signals:

- The hyperfine splitting occurs, if the spin S of an unpaired electron interacts with a nuclear spin I in the vicinity
- In this case, the Hamiltonian of the electron spins S contains an additional term for the hyperfine splitting

$$H = \mu_B S_z \bar{g} B_0 + I A S$$

with the hyperfine coupling tensor A

- If the Zeeman interaction of the electron spins S is the dominating interaction, the energy levels can be described by

$$E = \mu_B m_s \bar{g} B_0 + m_l A m_s$$

- For unpaired electrons of $^{55}\text{Mn}^{2+}$ atoms in an ionic solution or solid, the isotropic hyperfine coupling tensor is replaced by a factor of $A = -8.9 \times 10^{-3}$ cm^{-1} , $A/g\mu_B = 9.5 \text{ mT}$ or $A/h = 266 \text{ MHz}$: → Fig. 8.13

Experimental technique (L8, p. 36): → Fig. 8.14

- Most of the EPR spectrometers are an equipment with a sweeping magnetic field, a constant frequency device, and a resonator, which is optimized for this frequency (quality factor of $Q \geq 5000$)
- This resonator is a waveguide (like in Radar technique) coupled with a microwave generator, called klystron
- The sample is inside the resonator and causes a field dependent absorption and reflection of the irradiated microwaves, which are detected via a diode
- In the case of field-sweep EPR spectrometers, the scanning of the signal is performed by a linear increase or decrease (sweep) of the external magnetic B_0 field

Frequency ranges of EPR spectrometers:

- For a survey on the typical frequency ranges of EPR spectrometers, see: → Tab. 8.3
- Standard EPR spectrometers work in the so-called X band corresponding to a electron spin resonance frequency of ca. 9.5 GHz and a wavelength of ca. 3 cm
- The required flux density of the external magnetic field is 0.35 T, which can be easily reached with an iron magnet

EPR resonator:

- The size of an EPR resonator correlates with the wavelength
- Mostly, metal boxes covered inside by silver are used with the sample tube inserted via a hole (causes a detuning of the resonator)
- In the case of in situ experiments, a fixed bed reactor made by glass is installed inside the resonator
- This equipment can also contain a glass-fiber optics for simultaneous UV/Vis and/or Raman spectroscopy (A. Brückner et al., *Catal. Today* 113 (2006) 16): → Fig. 8.15

Sensitivity of EPR spectroscopy:

- Due to the significantly higher gyromagnetic ratio of the electron spins in comparison with those of the nuclear spins, EPR spectroscopy is orders of magnitude more sensitive than NMR spectroscopy at the same external magnetic B_0 field
- The minimum electron spin concentration N_{\min} , which can be detected by EPR spectroscopy depends on the microwave power P , the Larmor frequency ω_0 , the quality factor Q of the resonator, the sample filling factor η of the resonator, the line width $\Delta\omega$ and temperature T of the sample material, the noise temperature T^* and the bandwidth $\Delta\nu$ of the equipment, according to:

$$N_{\min} \approx kT \frac{\Delta\omega}{\omega_0} \frac{1}{\eta Q} \sqrt{\frac{kT^* \Delta\nu}{P}}$$

- Using a X band spectrometer, DPPH (α,α' -diphenyl- β -pikryl-hydrazyl) can be detected with a minimum electron spin number of 10^{10} , if the other parameters are: Time constant 10 s corresponding to a band width of $\Delta\nu = 0.1$ Hz, $T^* = 300$ K, signal linewidth of $\Delta B = 0.2$ mT, $Q = 5000$, $\eta = 0.4$, $P = 10$ mW

Reference materials for EPR studies (L8, p. 37):

- An often used standard (vide infra) is DPPH (α,α' -diphenyl- β -pikryl-hydrazyl): → Fig. 8.16, top, left
- This material has an EPR linewidth of ca. 0.2 mT, is a free radical with $g = 2.0036$, which is very near to the g factor of free electrons ($g_0 = 2.002322$)
- A more narrow EPR signal is caused by the radical anion salt $(FA)_2PF_6$, where FA stands for fluoranthene ($C_{16}H_{10}$): → Fig. 8.16, top, right
- At $T = 200$ to 300 K, this material gives an EPR signal with a linewidth of $\Delta B = 1.0$ to 1.5 μ T and has a g tensor of $g_1 = 2.00226$, $g_2 = 2.00258$, and $g_3 = 2.00222$, which is very close to $g_0 = 2.002322$

8.3.2 Application of EPR spectroscopy

EPR studies on the location and accessibility of Cu^{2+} cations in zeolite ZSM-5 (A.V. Kucherov et al., *Zeolites* 5 (1985) 320):

- Preparation of zeolites Cu-ZSM-5 (also used for the exhaust cleaning of Otto engines) by an exchange of the H⁺ form with copper nitrate and calcination at 823 K
- EPR measurements at 77 K on an X band spectrometer with a cell similarly to that shown in Fig. 8.15, however, without glass-fiber optics
- Before the studies, the samples were treated at 673 K in O₂ and, subsequently, evacuated at 298 K: → Fig. 8.17
- The EPR spectrum consists of two signals due to two different Cu²⁺ species with axial symmetry and hyperfine splitting: → Tab. 8.4
- The hyperfine splitting is caused by an interaction of the electron spins with the nuclear spins ($I = 3/2$) of ^{63/65}Cu isotopes
- Upon addition of molecular oxygen, a reversible broadening of the EPR signals occurs, which hints to the accessibility of the Cu²⁺ cations in the 10-ring pores of zeolite ZSM-5

Quantitative EPR studies of the reaction of Cu²⁺ cations in zeolites Cu-ZSM-5 with CH₄ (A.V. Kucherov et al., *Zeolites* 15 (1995) 15):

- Zeolite sample and EPR equipment like in the above-mentioned example
- Addition of MnO/Al₂O₃ powder as internal standard in the sample materials
- Mn²⁺ ions cause six very narrow EPR signals, which allow the determination of the copper concentration with an accuracy of ±5 %
- The EPR spectra recorded before and after changing the feeds from O₂ in He to CH₄ in He show significantly different intensities: → Figs. 8.18a-c
- Quantitative evaluation indicates a slow decrease and rapid increase of the EPR signals for purging with CH₄ and O₂ (both 10 ml/min), respectively: → Fig. 8.19
- In situ EPR experiments support the reversibility of reduction and oxidation of the Cu²⁺ species in zeolite Cu-ZSM-5

In situ EPR studies of the temperature dependence of V⁴⁺ species during the conversion of vanadylphosphathemihydrate into vanadylpyrophosphate (A. Brückner et al., *Catal. Today* 32 (1996) 215):

- The precursor VOHPO₄ · 0.5 H₂O was prepared by V₂O₅ and H₃PO₄ in an alcoholic solution

- The EPR measurements were performed under vacuum with a cell like shown in Fig. 8.15 (without glass-fiber optics) using an X band spectrometer
- EPR signals obtained at 373 K are due to interconnected VO^{2+} dimers: → Fig. 8.20, left
- With increasing dehydration temperature, the EPR signals are significantly broadened, which is caused by the formation of ladder-like double-chains of VO_6 units: → Fig. 8.20, left

In situ EPR studies on the oxidation state of vanadium in an amorphous VPO catalyst during the selective oxidation of *n*-butane (A. Brückner et al., *Catal. Today* 32 (1996) 215):

- The V^{4+} -containing pyrophosphate, which is EPR sensitive, was prepared by *n*-butane conversion at V^{5+} -containing vanadylorthophosphate (VOPO_4), which is not EPR sensitive
- The EPR measurements were performed under flow conditions (synthetic air with 300 ml/h and 1.5 vol.-% *n*-butane) in a cell like shown in Fig. 8.15 (without glass-fiber optics) using an X band spectrometer
- Upon increasing the temperature from 295 to 760 K, an increasing broad signal of V^{4+} species due to pyrophosphate was observed in the EPR spectra: → Fig. 8.21, top
- This EPR signals become narrow 18 days after the catalytic experiment, i.e., there is a slow reorientation of the framework oxygen in the local structure of the vanadium atoms: → Fig. 8.21, bottom

9. Solid-state NMR spectroscopy

9.1 Basics of solid-state NMR spectroscopy

General remarks (L8, p. 4):

- Nuclear magnetic resonance (NMR)
- Caused by the Zeeman interaction of nuclear spins I in an external magnetic B_0 field
- Nuclear spins I are characterized by a magnetic dipole moments μ

$$\mu = -\gamma \hbar I$$

which interact with the flux density B_0 of the magnetic field

and have the energy

$$E = \gamma \hbar I_z B_0 = m \hbar \omega_0$$

with the gyromagnetic ratio γ of the resonant nuclei, the z -component I_z of the nuclear spin operator I , the magnetic quantum number m , and the Larmor frequency ω_0

- According to the classical description, nuclear dipoles rotate with the Larmor frequency ω_0 on a conical path around the z -axis, which corresponds to the direction of the magnetic B_0 field: → Fig. 9.1, left
- According to the quantum-mechanical description, a splitting of the energy levels corresponding to the magnetic quantum numbers $m = +1/2$ and $-1/2$ occurs for spins $I = 1/2$: → Fig. 9.1, right
- Via irradiation of a radio frequency pulse, the magnetization is moved by 90° ($\pi/2$ pulse) from the B_0 -direction (classic picture), which corresponds to transitions between the energy levels are excited (quantum-mechanic picture), both causing a time-dependent nuclear polarization
- The free induction decay, $G(t)$, of the above-mentioned polarization is recorded; the Fourier transformation of $G(t)$ gives the NMR spectrum, $F(\omega)$, in the frequency domain: → Fig. 9.2
- The total magnetization M of a sample (proportional to the NMR signal intensity) is given by

$$M = N \frac{\gamma^2 \hbar^2 I(I+1)}{3k_B T} B_0 \quad (\text{Curie's law})$$

with the total number N of the spins I , the temperature T of the sample, and the Boltzmann constant k_B

Solid-state interactions of nuclear spins (L4, p. 201):

- In addition to the Zeeman interaction, the following internal nuclear interactions affect the positions, shapes, and linewidths ($\Delta \nu_{1/2}$) of solid-state NMR signals:
 - anisotropic chemical shielding caused by the electrons around the resonating nuclei with signal broadening of $\Delta \nu_{1/2} \leq 5 \times 10^3 \text{ s}^{-1}$
 - dipolar interaction with neighbouring nuclear dipole moments with signal broadening of $\Delta \nu_{1/2} \leq 5 \times 10^4 \text{ s}^{-1}$

- quadrupolar interaction of nuclei having a spins $I > \frac{1}{2}$ and an electric quadrupole moment with electric field gradients leading to signal broadenings of $\Delta\nu_{1/2} \leq 10^7 \text{ s}^{-1}$
- Often, the J-coupling (scalar coupling) is too weak for an observation in solid-state NMR spectra

Description of the chemical shielding anisotropy (CSA): → Fig. 9.3

- Electrons around the resonating nuclei cause a shielding of the external magnetic B_0 field, which decreases the magnetic field strength at the site of the nuclei
- The frequency distribution function of CSA is given by:

$$\omega = \omega_0[(1-\sigma_{\text{iso}}) - \Delta\sigma_{\text{CSA}} \left(\frac{3\cos^2\beta - 1}{2} + \frac{\eta_{\text{CSA}}}{2} \sin^2\beta \cos 2\alpha \right)]$$

with the isotropic shielding σ_{iso} , the anisotropy $\Delta\sigma_{\text{CSA}}$, and the asymmetry parameter η_{CSA} :

$$\sigma_{\text{iso}} = \frac{1}{3} (\sigma_{x'x'} + \sigma_{y'y'} + \sigma_{z'z'}) ; \quad \Delta\sigma_{\text{CSA}} = (\sigma_{z'z'} - \sigma_{\text{iso}})$$

$$\eta_{\text{CSA}} = \frac{(\sigma_{y'y'} - \sigma_{x'x'})}{\Delta\sigma}$$

and the Euler angles α and β describing the orientation of the shielding tensor given in the molecular frame x',y',z' relative to the laboratory frame x,y,z

- For the signal shapes in the case of different principal axis values σ_{ij} (general case) and two equal principal axis values (axial symmetry), see: → Fig. 9.3, bottom, left and right, respectively
- The values of $\Delta\sigma_{\text{CSA}}$ and η_{CSA} give information on chemical bonds in the local structure of the resonating nuclei

Description of dipolar interactions: → Fig. 9.4

- Neighbouring nuclear dipoles of nuclei with spin S influence the magnetic field at the site of the resonating nuclei with spin I
- The frequency distribution function of the dipolar interaction of non-equivalent nuclear spins I and S (heteronuclear dipole-dipole interaction) is given by:

$$\omega = \omega_0 \pm \frac{1}{2} \omega_D (1 - 3\cos^2\beta_{ik})$$

with $\omega_D = (\gamma_I \gamma_S \hbar \frac{\mu_0}{4\pi}) / r_{ik}^3$

for the interacting nuclei i and k in a distance r_{ik}

- For signal shapes of single crystals (angle β is fixed) and powder samples (angle β covers all possible values), see: → Fig. 9.4, bottom, left and right, respectively
- The value of ω_D give information on the distances of interacting nuclei i and k

Description of the quadrupolar interactions: → Fig. 9.5

- Nuclei with spins $I > 1/2$ are characterized by an electric quadrupole moment Q since their nuclei have a slightly elliptical shape leading to a non-spherical charge distribution
- The electric quadrupole moment Q interacts with the z' -component of the electric field gradient tensor $V_{z'z'} = eq$ at the sites of the resonating nuclei, e.g., caused by an inhomogeneous charge distribution in the local structure
- In this case, the distances of the nuclear energy levels responsible for the central and satellite transitions are not equidistant: → Fig. 9.5, top
- The frequency distribution function of the central transition ($m_l = -1/2 \Leftrightarrow +1/2$) is given by:

$$\omega_{-1/2,1/2} = -\frac{\omega_Q^2}{6\omega_0} \left[I(I+1) - \frac{3}{4} \right] (A \cos^4 \beta + B \cos^2 \beta + C)$$

with

$$A = -\frac{27}{8} - \frac{9}{4} \eta_Q \cos 2\alpha - \frac{3}{8} \eta_Q^2 \cos^2 2\alpha$$

$$B = +\frac{15}{4} - \frac{1}{2} \eta_Q^2 + 2\eta_Q \cos 2\alpha + \frac{3}{4} \eta_Q^2 \cos^2 2\alpha$$

$$C = -\frac{3}{8} + \frac{1}{3} \eta_Q^2 + \frac{1}{4} \eta_Q \cos 2\alpha - \frac{3}{8} \eta_Q^2 \cos^2 2\alpha$$

the quadrupole frequency ω_Q , quadrupole coupling constant C_Q :

$$\omega_Q / 2\pi = \frac{3e^2 q Q}{2I(2I-1)h} = \frac{3C_Q}{2I(2I-1)}$$

and the asymmetry parameter η_Q :

$$\eta_Q = \frac{V_{x'x'} - V_{y'y'}}{V_{z'z'}}$$

with the diagonal elements $V_{i'i'}$ of the electric field gradient tensor

- The above-mentioned frequency distribution function $\omega_{-1/2,1/2}$ contains in the laboratory frame the two geometry terms $(1 - 3\cos^2\beta)$ and $(35\cos^4\alpha - 30\cos^2\alpha + 3)$
- For signal shapes of single crystals (angles α and β are fixed) and powder samples (angles α and β cover all possible values), see: → Fig. 9.5, bottom, left and right, respectively
- The values ω_Q (or C_Q) and η_Q give information on the symmetry of the charge distribution in the local structure of the resonating nuclei

9.2 Experimental technique of solid-state NMR spectroscopy

Spectrometers (L8, p. 8): → Fig. 9.6

- The spectrometer consists of a radio frequency generator, a pulse modulator, a high-power amplifier, preamplifier box with diode switch, a probe head (inside the magnetic B_0 field), a phase-sensitive receiver, and a computer for accumulating the free induction decays and for their evaluation
- The diode switch directs the excitation pulse from the high-power amplifier to the probe and the received NMR signal from the probe to the preamplifier and the receiver: → Fig. 9.7, top
- NMR probe heads contain a resonance circuit with a quality factor of $Q \geq 100$, consisting of the coil around the sample tube and capacitors C and C' for tuning and matching, respectively: → Fig. 9.7, bottom

Experimental methods of high-resolution solid-state NMR spectroscopy (L6, p. 154; L7, p. 912):

a) Multiple-pulse sequences: → Fig. 9.8

- Averaging of the geometry term $(1 - 3\cos^2\beta)$ of the homonuclear dipolar I/I interaction by irradiation of multiple-pulse sequences, which move the magnetization vector along the x -axis and y -axis and back to the z -axis for same periods corresponding to a rotation around the $[1,1,1]$ axis

- Since the [1,1,1] axis stands in an angle of $\beta = 54.7^\circ$ ($\text{arc cos}(\sqrt{1/3})$) to the B_0 field, the term $(1 - 3\cos^2\beta)$ becomes zero and the line broadening disappears
 - This method does not require a mechanical spinning of the sample, but is limited to an averaging of homonuclear dipolar interactions
- b) Rapid sample spinning around an axis in the magic angle (MAS): → Fig. 9.9
- Mechanical rotation of the sample around an axis in the magic angle of $\beta_m = 54.7^\circ$ averages the term $(1 - 3\cos^2\beta)$ for all kind of nuclear spin interactions
 - The spinning frequency ν_{rot} should be larger than the NMR linewidth obtained without MAS
 - Turbines with an air bearing system reach sample spinning frequencies of ca. 6 kHz for 7 mm, 15 kHz for 4 mm, and 32 kHz for 2.5 mm MAS rotors
 - Can be applied on all interactions with Hamiltonians containing exclusively the geometry term $(1 - 3\cos^2\beta)$, i.e., anisotropic chemical shielding and dipolar interactions
 - In the case of quadrupolar interactions, the narrowing by magic angle spinning (MAS) is limited to a factor 1/3.6 since the corresponding Hamiltonian consists of two geometry terms (vide supra)
- c) Double oriented rotation (DOR): → Fig. 9.10
- Averaging of the two geometry terms $(1 - 3\cos^2\beta)$ and $(35\cos^4\alpha - 30\cos^2\alpha + 3)$ by a simultaneous sample spinning around two axes in the angles of $\beta = 54.7^\circ$ and $\alpha = 30.6^\circ$
 - In the case of DOR, a small rotor (ν_{rot} ca. 7 kHz) spins inside a large rotor (ν_{rot} ca. 1.5 to 2.5 kHz), which is surrounded by the coil (bad sample filling factor, small spinning frequency of the outer rotor)
 - This technique can be used for averaging quadrupolar interactions of sample, which have no strong dipolar interactions (low spinning speed), but high signal intensities (bad filling factor)
- d) Two-dimensional (2D) multiquantum MAS NMR spectroscopy (2D MQMAS): → Figs. 9.11 and 9.12
- In a two-dimensional (2D) experiment, the time period t_1 is utilized to scan an interaction by a stepwise increase of t_1 (gives $(G(t_1))$)

- The information on this interaction is included in the free induction decays, which are recorded in the time period t_2 at the end of the pulse experiment (gives $G(t_1, t_2)$)
- A twofold Fourier transformation of $G(t_1, t_2)$ gives the two-dimensional spectrum $F(\nu_1, \nu_2)$ with the information scanned during t_1 along the ν_1 -axis and the classical spectra (like 1D spectra) recorded during t_1 along the ν_2 -axis
- In the case of a MQMAS experiment, the 2D technique is used for studying multiquantum (MQ) transitions of quadrupolar nuclei during the time period t_1 (no broadening of the signals by quadrupolar interactions along the ν_1 -axis of the 2D spectrum)
- 2D MQMAS NMR spectra show signals with quadrupolar broadening along the ν_2 -axis (like 1D MAS NMR spectrum) and strongly narrowed signals along the ν_1 -axis (without quadrupolar broadening)

Experimental technique of in situ MAS NMR spectroscopy (L6, p. 160; L7, p. 1014):

a) High-temperature MAS NMR probe head: → Fig. 9.13

- Heating by hot bearing gas (high thermal noise due to the hot coil) or by a Laser beam (CO_2 Laser with a power of 50 to 100 W)
- Temperatures of up to 873 K
- The signal/noise ratio is limited due to Curie's law

b) External activation and preparation of the catalysts: → Fig. 9.14

- Use of equipments for the activation of catalysts in vacuum and for their loading with probe molecules or reactants
- Transfer of the pretreated catalysts inside the MAS rotor without air contact (no rehydration) into the magnetic B_0 field

c) In situ MAS NMR spectroscopy under flow conditions: → Fig. 9.15

- Catalysts are pressed to a hollow cylinder inside the MAS rotor, which allows the insertion of an injection tube into the rotor via a hole in the rotor cap
- Via this injection tube, gaseous reactants can be injected into the sample volume filled with the activated catalysts during the MAS NMR measurement

d) Combination of various in situ techniques for the study of working catalysts

(operando): → Figs. 9.15 and 9.16

- The MAS rotor has a quartz glass window at the bottom and a glass-fiber optics is installed at the bottom of the stator

- Suitable for simultaneous in situ MAS NMR and UV/Vis spectroscopic investigations of working solid catalysts

9.3 Application of solid-state NMR spectroscopy

^{29}Si MAS NMR studies on the incorporation of metal atoms into the framework of silicate-type catalysts and adsorbents (L4, p. 216):

- ^{29}Si isotopes have a nuclear spin $I = 1/2$ with the natural abundance of 4.7 %
- Mostly, ^{29}Si MAS NMR studies are performed without an isotopic enrichment
- Positions of the ^{29}Si MAS NMR signals caused by crystalline aluminosilicates depend on the framework aluminum content → Fig. 9.17, top
- Study of totally dealuminated sample allow the identification of the ^{29}Si MAS NMR signals due to silicon atoms at crystallographically non-equivalent positions, → Fig. 9.17, bottom
- The chemical shifts δ_{Si} (reverse to $-\sigma_{\text{iso}}$) give the number n of aluminum atoms coordinated via oxygen bridges to the resonating $\text{Si}(n\text{Al})$ species: → Tab. 9.1 and Fig. 9.18
- The intensities $I_{\text{Si}(n\text{Al})}$ of the $\text{Si}(n\text{Al})$ signals ($n = 0$ to 4) are used for calculating the framework $n_{\text{Si}}/n_{\text{Al}}$ ratio via:

$$n_{\text{Si}}/n_{\text{Al}} = \sum_{n=0}^4 I_{\text{Si}(n\text{Al})} / \sum_{n=0}^4 0.25 \cdot n \cdot I_{\text{Si}(n\text{Al})}$$

- NMR is the solely method for this task due to its high sensitivity for local structures (short range method)

^{29}Si MAS NMR studies of the Si-O-Si connectivities in zeolite framework by two-dimensional experiments (L4, p. 222):

- The COSY (COrelatEd SpectroscopY) pulse group consists at first by a cross polarization sequence for transferring nuclear polarization from abundant ^1H nuclei to rare ^{29}Si nuclei (enhances the ^{29}Si NMR signals): → Fig. 9.19a
- This part of the sequence is followed by a evolution period in the time period t_1 , a $\pi/2$ pulse, and the detection period t_2
- The twofold Fourier transformation of $G(t_1, t_2)$ gives the 2D spectrum with signals of silicon atoms on crystallographically non-equivalent positions at the diagonal: → Figs. 9.19b and 9.19c

- If two silicon atoms are directly connected via an oxygen bridge, the bond electrons of these atoms cause a J-coupling (indirect spin-spin coupling) and cross peaks away from the diagonal occur in the 2D spectrum: → Fig. 9.19d

Correlation of the chemical shift $\delta_{29\text{Si}}$ with crystallographic parameters (L4, p. 220):

- The chemical shifts $\delta_{29\text{Si}}$ correlate with the distances r_{OT} and r_{OTO} as well as the Si-O-T bond angle α
- Often used correlations are:

$$\delta_{29\text{Si}} / \text{ppm} = 5.230 - 0.570 \alpha$$

$$\delta_{29\text{Si}} / \text{ppm} = 223.9 \cos\alpha / (\cos\alpha - 1) + 5n - 7.2$$

with the number n of the aluminum atoms in the first coordination sphere of T atoms

- These correlations allow the validation of calculated structure models obtained by XRD investigations via comparison of theoretical δ_{Si} values (calculated using the Si-O-T bond angles α) with experimentally obtained ^{29}Si MAS NMR spectra: → Fig. 9.20

^{27}Al MAS NMR studies of the oxygen coordination of aluminum atom in aluminosilicates (L4, p. 224; L. 7, p. 921):

- ^{27}Al isotopes have a natural abundance of 100 % and a spin $I = 5/2$ (quadrupolar nuclei) with high electric quadrupole moment Q (strong signal broadening)
- Via the chemical shifts of the ^{27}Al MAS NMR signals, the oxygen coordination number (Al^{III} , Al^{IV} , Al^{V} , Al^{VI}) can be distinguished: → Fig. 9.21
- Often, the strong quadrupolar interactions of ^{27}Al nuclei (broadening of signals) can be significantly decreased by a full hydration of the sample under study, which decreases the electric field gradient in the local structure: → Fig. 9.22, left
- Application of cross polarization (CP) experiments allows the identification of aluminum species coordinated to water molecules ($^1\text{H} \Leftrightarrow ^{27}\text{Al}$): → Fig. 9.22, right

^{27}Al MAS NMR studies of the nature of aluminum species in dehydrated aluminosilicates (J. Jiao et al., *Phys. Chem. Chem. Phys.* 7 (2005) 3221):

- No rehydration of the H-Y zeolites after their dealumination in under water vapour and subsequent purging in dry nitrogen
- Samples were studied by ^{27}Al spin-echo NMR, high-speed MAS NMR, and MQMAS NMR spectroscopy in magnetic fields of $B_0 = 9.4$ to 17.6 T
- Comparison of ^{27}Al spin-echo and MAS NMR spectra demonstrates the narrowing effect of the MAS technique (1 divided by 3.6): → Fig. 9.23
- Because of the strong overlap of signals, the simulation of 1D spectra requires additional information (number of signals, chemical shifts $\delta_{27\text{Al}}$, quadrupolar coupling constants C_q), which can be obtained by MQMAS NMR spectroscopy → Fig. 9.24
- Subsequent, quantitative evaluation of the relative intensities can be performed by separation of the 1D spectra using the parameters:
 - signal 1: $\delta_{27\text{Al}} = 70 \pm 10$ ppm $C_q = 15.0 \pm 1.0$ MHz $I = 48$ %
 - signal 2: $\delta_{27\text{Al}} = 65 \pm 5$ ppm $C_q = 8.0 \pm 0.5$ MHz $I = 27$ %
 - signal 3: $\delta_{27\text{Al}} = 35 \pm 5$ ppm $C_q = 7.5 \pm 0.5$ MHz $I = 21$ %
 - signal 4: $\delta_{27\text{Al}} = 10 \pm 5$ ppm $C_q = 5.0 \pm 0.5$ MHz $I = 4$ %
- For details of the evaluation of MQMAS NMR spectra, see J. Rocha et al., *Top. Curr. Chem.* 246 (2004) 141

^1H MAS NMR studies on surface OH groups acting as Brønsted acid sites of solid catalysts (L4, p. 253; L7, p. 1163):

- ^1H isotopes have a spin $I = \frac{1}{2}$ with a natural abundance of 100 %
- Before the ^1H MAS NMR measurements, the samples under study must be completely dehydrated; otherwise, the spectra are dominated by strong water signals
- ^1H MAS NMR signals of the different types of OH groups have characteristic shift ranges: → Fig. 9.25, Tab. 9.2
- The ^1H NMR shifts $\delta_{1\text{H}}$ of OH groups correlate with the wavenumbers $\tilde{\nu}_{OH}$ of the stretching vibrations

$$\delta_{1\text{H}} / \text{ppm} = 57.1 - 0.0147 \tilde{\nu}_{OH} / \text{cm}^{-1}$$

- In the case of hydrogen bondings of the hydroxyl protons to neighboring oxygen atoms (indicated in Tab. 9.2 by an apostrophe), a low-field resonance shift $\Delta\delta_{1\text{H}}$ occurs:

$$\Delta\delta_{1\text{H}} = 79.05 - 0.255 d_{\text{OH-O}} / \text{pm}$$

with the O-O distance $d_{\text{OH-O}}$ of the hydrogen bond in picometer

- The dipolar coupling between hydroxyl protons can be investigated by two-dimensional spin-exchange experiments, which evaluate the transfer of polarization between the neighbouring ^1H nuclei in the time period Δ : → Fig. 9.26
- Twofold Fourier transformation leads to 2D spectra with cross peaks, which are due to dipolarly coupled ^1H nuclei with short distances: → Fig. 9.27

Characterization of the pore system in porous solids via ^{129}Xe NMR spectroscopy (L4, p. 272):

- ^{129}Xe isotopes have a spin $I = 1/2$ with a natural abundance of 26.4 %
- The experimentally observed chemical shifts, $\delta_{129\text{Xe}}$, of xenon atoms adsorbed in porous solids are described by:

$$\delta_{129\text{Xe}} = \delta_0 + \delta_S + \delta_E + \delta_M + \delta_{\text{Xe-Xe}} \rho_{\text{Xe}}$$

with the chemical shift δ_0 of the free xenon gas, the chemical shift δ_S of xenon atoms in pores at a pressure of zero, the chemical shift δ_E of xenon atoms in strong electrostatic fields (caused by extra-framework cations), the chemical shift δ_M of xenon atoms adsorbed at metals, and the resonance shift $\delta_{\text{Xe-Xe}}$ due to xenon-xenon collisions depending on the density ρ_{Xe} of xenon atoms

- The collisions of xenon atoms with the pore walls in micro- and mesopores cause a modification of the shielding of the ^{129}Xe nuclei by their electrons leading to a chemical shift
- If the shift $\delta_{129\text{Xe}}$ is evaluated for a xenon pressure extrapolated to zero and using porous solids free of cations and metal sites, the shift value correlates with the pore diameter: → Fig. 9.28 and Tab. 9.3

In situ MAS NMR studies of the heterogeneous catalyzed methanol-to-olefin conversion under flow conditions (Y. Jiang et al., *Microporous Mesoporous Mater.* 105 (2007) 132):

- Application of an in situ MAS NMR-UV/Vis probe head according to Fig. 9.15

- Reaction under flow conditions ($W/F_{\text{me}} = 25 \text{ g}/\text{mol}$) on a porous (8-ring pores) silicoaluminophosphate SAPO-34, with a catalyst mass of 100 mg, and using ^{13}C -enriched methanol (enrichment 99 %) as reactants
- Measurements were performed on a 400 MHz NMR spectrometer and using a glass-fiber UV/Vis spectrometer Avantes HPSUV1000A, and an AvaLight-DH-S-Deuterium light source
- UV/Vis investigation of bands due to $\pi-\pi^*$ transitions, which are due to protonated dienes (245 nm), aromatics (280 nm), di- and trienylic carbenium ions (345, 430 nm), and polycyclic aromatics, i.e., coke (400 nm): → Fig. 9.29
- Signals in the simultaneously recorded ^{13}C MAS NMR spectra:
 - $\delta_{^{13}\text{C}} = 50 \text{ ppm}$: methanol
 - $\delta_{^{13}\text{C}} = 61 \text{ ppm}$: dimethylether (DME)
 - $\delta_{^{13}\text{C}} = 13-31 \text{ ppm}$: various alkanes and alkyl chains
 - $\delta_{^{13}\text{C}} = 125-135 \text{ ppm}$: various polyalkylaromatics
- Conversion of methanol to DME dominates at low reaction temperatures
- With increasing reaction temperature and time-on-stream, at first aromatics are formed (hydrocarbon pool), while later the band of coke occurs at 400 nm (deactivation of the catalyst)
- Signals at 18 ppm and 125-135 ppm indicate the formation of polyalkylated benzene
- Studies support results of quantum-chemical calculations, which indicated that hexamethylbenzene is a highly reactive compound in the hydrocarbon pool formed on the MTO catalyst SAPO-34

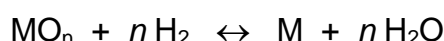
10. Thermal surface characterization methods

10.1 Temperature-programmed reduction (TPR)

10.1.1 Basics of temperature-programmed reduction

General remarks (L2, p. 13):

- Reduction is necessary for the formation and activation of metal catalysts and is often performed in under flowing H_2



i.e., the reaction is affected by the partial pressures p_i of H_2 and H_2O

$$\Delta G = \Delta G^0 nRT \ln(p_{H_2O}/p_{H_2})$$

with a change of Gibb's free energy ΔG under standard conditions

- The reaction happens, if the ratio p_{H_2O}/p_{H_2} inside the reactor is smaller than the equilibrium level: → Tab. 10.1
- The phase diagram of iron indicates that only small contents of water already lead to a re-oxidation of the active metal compound: → Fig. 10.1
- During the TPR experiment, therefore, it is important that the formed water is rapidly removed
- In the case of a wrong reduction procedure, agglomeration of the metal compounds may occur, while well dispersed metal for high catalytic activity is required

Experimental technique:

- In the case of TPR measurements, the temperature must be found, at which the H_2 consumption starts, i.e. the reduction of the metals under study occurs
- The equipment consists of a reactor filled with the catalyst, which can be well-defined heated with rates of 0.1 to 20 K/min using a temperature-programmer
- Thermal conductance detectors (TCD) measure the H_2 contents before and after the reactor (H_2 consumption): → Fig. 10.2
- A dryer removes the water, which would affect the accuracy of the TCD results
- TPR studies are often performed with 5 vol.% H_2 in argon or helium

10.1.2 Application of the temperature-programmed reduction

TPR of rhodium, iron, and iron/rhodium chloride complexes on SiO_2 (L2, p. 18):

- Equipment like shown in Fig. 10.2
- Reduction was performed with 5 vol.% H_2 in helium of the fresh catalyst (TPR1) and after total oxidation of the catalyst (TPR2)

Following observations were possible: → Fig. 10.3

- a) - TPR curves of the fresh catalysts (TPR1) show two peaks

- Comparison of the TPR1 and TPR2 curves indicates that the low- and high-temperature peaks of the fresh Rh/SiO₂ catalyst are due to reduction of Rh-O and Rh-Cl bonds, respectively
 - In the case of the Fe/SiO₂ catalyst, the assignment of the peaks is reversed
- b) - The integrals of the TPR curves, which correspond to the amounts of consumed H₂, are much lower for iron (0.62 and 0.47) than for rhodium (1.45 and 1.52)
- The H₂/M ratio of ca. 1.5 for rhodium hints to the presence of rhodium in the form of Rh₂O₃
 - The low H₂/M ratio of ca. 0.5 for iron indicates that it was not completely reduced
- c) - The reduction temperature is for the more noble rhodium significantly lower than for iron
- The observed tendency agrees with the values given in Tab. 10.1, i.e., rhodium is easier to reduce than iron

10.2 Temperature-programmed sulfurization (TPS)

10.2.1 Basics of temperature-programmed sulfurization

General remarks (L2, p. 22):

- TPS is a modification of TPR and uses a gas mixture consisting of H₂S and H₂
- TPS is very important for the characterization of HDS catalysts (hydrodesulfurization) utilized for the desulfurization of oil cuts
- Often, Al₂O₃-supported molybdenum catalysts are used, which must be activated by sulfurization
- H₂ helps to prevent the decomposition of H₂S and the uncontrolled formation of sulphur deposits on the catalysts

Experimental technique (L2, p. 12):

- The TPS equipment is composed like shown in Fig. 10.2 or has a mass spectrometer for the gas analysis at the exhaust of the reactor: → Fig. 10.4

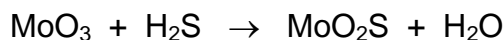
10.2.2 Application of temperature-programmed sulfurization

TPS studies of the temperature dependence of the sulfurization of $\text{MoO}_3/\text{Al}_2\text{O}_3$ catalysts (L2, p. 22):

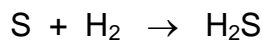
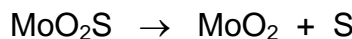
- Equipment like shown in Fig. 10.4 and analysis of H_2S , H_2 , and H_2O via mass spectrometer
- Negative peaks correspond to a consumption of gases, while positive peaks are due to the formation of gas compounds

Following observations were possible: → Fig. 10.5

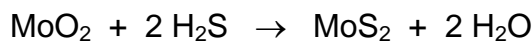
- a) - At ca. 400 K, H_2S is consumed (negative peak) and H_2O is formed (positive peak), while H_2 could not be detected
- This finding indicates that sulfur replaces oxygen in the catalyst



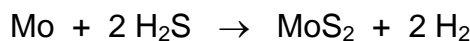
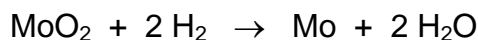
- b) - At ca. 500 K, the catalyst consumes a large amount of H_2 in a narrow temperature range (narrow peak), while H_2S and a small amount of H_2O are formed (negative peaks)
- The hydrogenation is explained by a surplus of sulfur, which is formed via the thermal decomposition of oxysulfides



- c) - Upon further increase of the temperature, H_2S is continuously consumed (broad negative peak) and H_2O is formed (broad positive peak)
- This finding indicates the replacement of the remaining oxygen atoms at the molybdenum by sulfur atoms



- This reaction can also occur in two steps



10.3 Temperature-programmed desorption (TPD)

10.3.1 Basics of temperature-programmed desorption

General remarks (L7, p. 1122):

- Is a routine method for the characterization of the nature and concentration of acid and base sites on the surface of solid catalysts

- For the study of acid sites, strong bases, such as ammonia and pyridine, are adsorbed on the activated catalysts and, subsequently, the weakly physisorbed molecules are desorbed at ca. 373 K
- The TPD measurement is performed during purging the base-loaded samples with an inert gas (often Ar or He) in a temperature range of 423 to 973 K
- For the characterization of base sites, CO_2 is used as probe molecule

Experimental technique (L2, p. 24):

- Equipment similar like used for TPR and TPS
- It consists of a fixed-bed reactor containing the catalyst, an oven for the activation of the catalyst before its loading with probe molecules, and for the temperature-programmed desorption: → Fig. 10.6
- Detection of the desorbed probe molecules via a thermal conductance detector (TCD), mass spectrometer, or gravimetrically
- Combination of the TPD method with FTIR spectroscopy in a single equipment, where the fixed-bed reactor is replaced by an IR cell (M. Niwa et al., *Microporous Mesoporous Mater.* 82 (2005) 105): → Fig. 10.7
- Allows the detailed assignment and investigation of adsorption sites

For the evaluation of TPD curves, see B. Hunger et al., *J. Therm. Anal.* 36 (1990) 1379:

- Depending on the procedure, TPD curves consist of a low-temperature peak (LT) and a high-temperature peak (HT): → Fig. 10.8
 - LT peak at ca. 473 K: physisorbed probe molecules
 - HT peak at 500 to 900 K: probe molecules chemisorbed at Brønsted and coordinated at Lewis acid sites
- Distinction of the nature (Brønsted or Lewis) of acid sites is not possible by TPD of ammonia or pyridine
- Doubtless identification of Brønsted acid sites requires the use of reactive amines (R.J. Gorte, *Catal. Lett.* 62 (1999) 1):
 - adsorption process
$$\text{R-CH}_2\text{-CH}_2\text{-NH}_2 + \text{ZOH} \rightarrow \text{R-CH}_2\text{-CH}_2\text{-NH}_3^+ \cdots \text{ZO}^-$$
 - desorption process



- The integrals of the desorption curves are proportional to the number of the corresponding surface sites on the catalysts under study (assuming that always one molecule per sites is adsorbed)
- The maximum temperature T_m of the HT peak gives the desorption energy E_d (L7, p. 1124)

$$E_d/R T_m^2 = (\nu_d/\beta) \exp\{-E_d/R T_m\} [F_s^0/(k_a p(1-\Theta_m)^2)]$$

with the frequency factor ν_d of the desorption, the heating rate β , the inert gas flow F_s^0 , the adsorption rate k_a , the partial pressure p , and coverage degree Θ_m at the desorption maximum, but the detailed values of these parameters are not known

- Often, the position T_m of the HT peak is used as a rough estimation of the acid strength of surface sites

10.3.2 Application of temperature-programmed desorption

TPD study of acidic zeolite catalysts (L. Yang et al., *Appl. Catal.* 67 (1991) 169): → Fig. 10.9

- Equipment like shown in Fig. 10.6
- Ca. 0.5 g of solid catalyst was dehydrated at 773 K for 1 h, loaded with ammonia (7.3 kPa) at 373 K for 45 minutes and, subsequently evacuated at 373 K for 45 minutes
- The temperature-programmed desorption was performed with a heating rate of 2.5 K/min at 343 to 773 K
- TPD properties of zeolite catalysts:
 - a) H-SAPO-5: $n_{\text{Si}}/(n_{\text{Si}}+n_{\text{Al}}+n_{\text{P}}) = 0.076$, $T_m = 514$ K, $n_{\text{HT}} = 0.4$ mmol/g
 - b) H-SAPO-11: $n_{\text{Si}}/(n_{\text{Si}}+n_{\text{Al}}+n_{\text{P}}) = 0.068$, $T_m = 548$ K, $n_{\text{HT}} = 0.35$ mmol/g
 - c) H-ZSM-5: $n_{\text{Si}}/n_{\text{Al}} = 25.3$, $T_m = 673$ K, $n_{\text{HT}} = 0.50$ mmol/g
- HT peaks occur in the temperature range of $T_m = 514$ to 673 K and the maximum temperature correlates well with the acid strength of the above-mentioned materials

- The integral of the HT peaks correspond to the number n_{HT} of the strong Brønsted acid sites of zeolites, i.e., of bridging OH groups (SiOHAl)
- For SAPO's, the n_{HT} values depend on the framework silicon contents, while for aluminosilicates (e.g. ZSM-5), the framework aluminum content is important

10.4 Microcalorimetry

10.4.1 Basics of microcalorimetry

General remarks (L7, p. 1126):

- Similar like the activation energy E_d of TPD in Section 10.3, also the adsorption heat of probe molecules at surface sites correlates with their acid or base strength
- The principle of microcalorimetry consists of the measurement of the adsorption heat via a microcalorimeter, which contains very sensitive pressure sensors for determining the amounts of adsorbed probe molecules
- Small amounts Δn_S of 1 to 10 μmol probe molecules are stepwise adsorbed at the activated catalysts and the differential adsorption heat q_{diff} is measured

$$q_{\text{diff}} = (\Delta Q / \Delta n_S)$$

with the adsorption heat ΔQ , determined for each pulse Δn_S of probe molecules

- The method allows the determination of the adsorption heat as a function of the number of adsorbed molecules

Experimental technique (L7, p. 1126):

- Microcalorimeters consist of:
 - calorimeter cell containing the sample
 - thermal block, which is a heat sink
 - thermal conductance detector between the sample container and the heat sink
- Often, microcalorimeters of the Tian-Calvet calorimeter type are used (A. Auroux, *Top. Catal.* 4 (1997) 71), which have a reference cell in addition to the sample cell, → Fig. 10.10

10.4.2 Application of microcalorimetry

Microcalorimetric determination of the adsorption heat and number of Brønsted acid sites of zeolites H-ZSM-5 with different framework aluminum contents (R.J. Gorte, D. White, *Top. Catal.* 4 (1997) 57): → Fig. 10.11

- Equipment like shown in Fig. 10.10
- Use of the base pyridine as probe molecule
- Plot of the differential adsorption heat q_{diff} as a function of the number n_a of adsorption sites
- Curves show a plateau at $q_{\text{diff}} \approx 200 \text{ kJ/mol}$
- This differential adsorption heat corresponds to those of strong Brønsted acid sites of zeolites, i.e., of bridging OH groups (SiOHAI)
- The drop down of the curves give the number of acid sites in the range of 180 to 600 $\mu\text{mol/g}$ for the different zeolites under study (depending on the aluminum content)

Comparison of the adsorption heats of different probe molecules and different types of zeolites:

- Use of the bases ammonia, pyridine, and isopropylamine as probe molecules adsorbed on the same zeolite H-ZSM-5 ($n_{\text{Si}}/n_{\text{Al}} = 20$): → Fig. 10.12
- The q_{diff} values depend on the basicities of the probe molecules and not on the amount of catalysts, i.e., the values are site specific
- Comparison of different zeolite catalysts demonstrates the influence of the zeolite type and the effect of the metals incorporated into the framework on the differential adsorption heat and acid strength: → Tab. 10.2

For a scale of the acid strength on the basis of the differential adsorption heat of ammonia, see A. Auroux, *Top. Catal.* 19 (2002) 205): → Fig. 10.13

- For zeolites with same structure type (e.g. zeolite Y), the strong effect of the framework aluminum content on the differential adsorption heat and acid strength is demonstrated